DEM investigation of mechanical behavior and strain localization of methane hydrate bearing sediments with different temperatures and water pressures

DEM investigation of mechanical behavior and strain localization of methane hydrate bearing sediments with different temperatures and water pressures

Mingjing Jiang [1,2,3], Di Peng [1,2,3], Jin Y. Ooi [4]

[1] *State Key Laboratory for Disaster Reduction in Civil Engineering, Tongji University, Shanghai 200092, China*

[2] *Department of Geotechnical Engineering, College of Civil Engineering, Tongji University, Shanghai 200092, China*

[3] *Key Laboratory of Geotechnical and Underground Engineering of Ministry of Education, Tongji University, Shanghai 200092, China*

[4] *Institute for Infrastructure and Environment, School of Engineering, The University of Edinburgh, Edinburgh EH9 3JL, United Kingdom*

Correspondence to: Dr. Mingjing Jiang, Professor of Geotechnical Engineering, "Professor of Exceptional Rank in Tongji University"
Tel: +86-21-65980238; Fax: +86-21-65980238.

E-mail: mingjing.jiang@tongji.edu.cn (Mingjing Jiang), di.peng.tongji@hotmail.com (Di Peng), j.ooi@ed.ac.uk (Jin Y. Ooi)

Abstract: This paper investigates the mechanical behavior and strain localization of methane hydrate bearing sediments (MHBS) at different temperatures and water pressures via the distinct element method (DEM). A thermo-hydromechanical contact model of MHBS has been employed in the DEM to simulate biaxial tests and mechanical behavior of MHBS is studied with different temperatures and water pressures. Three MHBS specimens are simulated at different temperature-pressure conditions to provide an insight on the evolution of macro and micro variables during strain localization of MHBS, as well as the geometric characteristics of shear band. The results show that MHBS appears to be strain-softening with dilatancy and the existence of MH will increase the cohesion but decrease the friction angle of MHBS. As temperature increases or water pressure decreases, the cohesion and friction angle of MHBS decrease with increasing dilatancy. The strain localization is closely related to bond breakage as well as localization of other micro and macro variables such as contact force chains, principal stress fields, particle velocity fields and average pure rotation rate distributions. As temperature and water pressure change, three different types of shear band can form. The thickness and inclination angle of these shear bands increase as the temperature increases or water pressure decreases.

Keywords: methane hydrate; mechanical behavior; strain localization; distinct element method; temperature and water pressure

1 Introduction

Methane hydrate (MH) is a solid clathrate compound in which large amounts of methane is trapped within the crystal structure of water. The storage of methane hydrate is twice that of petrol and methane, making MH a promising new potential energy in the 21st century. Methane hydrate bearing sediments (MHBS) are mixture containing soil skeleton with MH trapped in the voids. Improper extraction of MH may lead to failure of MHBS, causing serious geohazards, such as submarine landslide (Evans et al., 1996), seabed pipeline breakage (Wang et al., 2009), etc. Therefore it is crucial to study the mechanical behavior of MHBS to allow safe extraction of MH.

In the past decade, the mechanical behavior of MHBS has been intensely studied using laboratory tests and numerical simulations. Kataoka et al. (2009) conducted several physical and mechanical tests of MHBS taken from the bottom of lake Balkal and found the MHBS samples slightly different from the ordinary soils on physical properties but significantly different on shear strength and modulus. Masui et al. (2005) and Hyodo et al. (2007) studied the mechanical behavior of synthesized MHBS specimens and showed that the existence of MH, as well as the increase of MH saturation increases the strength of MHBS greatly. Santamarina and Ruppel (2010) conducted tests on synthetic tetrahydrofuran hydrate bearing soils and found that the increase of hydrate saturation increased the effect on physical and mechanical properties of synthetic samples. There are also numerical simulations (Ayoub et al., 2007; Ng et al., 2008) and research on the constitutive models (Yan et al., 2013;

Uchida et al., 2012) of MHBS. Since it is hard to conduct in-situ test on MHBS or take undisturbed samples of MHBS, the majority of the studies are based on synthesized specimens. Both in-situ tests and triaxial tests of synthesized specimens can capture the main mechanical behavior (i.e. strength and stress-strain relationship) of MHBS, and such behavior is also studied for MHBS at different MH saturations (Masui et al., 2005; Hyodo et al., 2007; Santamarina and Ruppel, 2010). The mechanical behavior of MHBS is deeply related to temperature and water pressure of MH (Li et al., 2012; Hyodo et al., 2013) which have not been deeply studied previously, though there are studies on MHBS with the effect of water pressure only (Jiang et al., 2015a). This limitation provides the first motivation for this paper.

Strain localization leading to the formation of shear bands is a precursor of failure in soils associated with instability of embankments, slopes, dams and excavations in geotechnical engineering (Jiang et al., 2010). Previous studies appear to have focused on the mechanical response of MHBS without paying much attention to the process of gradual breakage of MHBS. There is thus a lack of understanding in the evolution of the stress and the ensuing breakage of MH bonds in the test specimens. In this paper, the distinct element method (DEM), originally developed by Cundall and Strack (1979), is adopted to investigate the micro and macro mechanical behavior as well as the strain localization of MHBS subject to triaxial testing condition. DEM models the soil as an assembly of particles, solving the Newton's kinematic laws for particle motion and a constitutive law at particle contact. It computes the microscopic response of the assembly from which the macroscopic response can be calculated.

DEM has been proven to be a powerful tool in studying geotechnical problems, such as developing constitutive model and mechanical response of sandy grains (Jiang et al., 2005, 2014c; Zhou and Ooi, 2009), mechanism in penetration tests (Jiang et al., 2006, 2014d), strain localization of cemented granules (Jiang et al., 2013b) or granular materials (Jiang et al., 2015b), strength theories of unsaturated soils (Jiang et al., 2004), mechanical behavior of lunar soils (Jiang et al., 2013a, 2014e; Chung and Ooi, 2008). As for DEM studies of MHBS, the strength, stiffness and dilatancy, along with the effect of MH saturation, have been studied previously (Jiang et al., 2014a; Jung et al., 2012; Holtzman, 2009; Brugada et al., 2010; Yu et al., 2012). Contact model of MHBS incorporating surface tension was proposed by Kreiter et al. (2007) to study the mechanical behavior where the influence of MH saturation was investigated thoroughly. In addition, submarine landslide of MHBS was simulated via a coupled approach with computational fluid dynamics (CFD) and DEM (Jiang et al., 2015c).

In the revised manuscript, the revision is included and highlighted in red font in Page 5-6. “The earlier study (Jiang et al., 2014a) presented a preliminary MH bond contact model that was based on bond contact experiments. However, the model only considered contact pairs where the particles were physically in contact; for those contact pairs where the particles were not in contact, no MH bond could form. The simpler model was further enhanced in Jiang et al. (2014b) where a “thickness” parameter was introduced allowing the MH bond to form when the gap between two particles was less than a critical length parameter. Therefore, the first objective of this

paper is to combine these two types of contacts and made a unified force-displacement interpretation (Eq. (2)) for the new DEM model adopted in this study. Furthermore in this study, we combined the temperature and water pressure to a unified parameter L for simplicity, compared with Jiang et al. (2014a, 2014b). The improved thermo-hydro-mechanical MH contact model in this study is then employed to conduct DEM simulations of biaxial tests on MHBS with different temperatures and water pressures using the *PFC2D* code (version 3.10) and to analyze the mechanical behavior as well as the micro and macro variables of MHBS specimens during strain localization. The results show that the basic mechanical properties predicted in the present DEM study correspond to those observed in laboratory tests. In addition, the microscopic features inside and outside of shear band are studied in detail. Different types of MH bond breakage have also been revealed in this study, which is considered to be probably the reason for different types of shear bands that appeared in previous experimental (Yoneda et al., 2011) and numerical studies (Jiang et al., 2014a; Stegmann et al., 2011). This paper provides a new insight into strain localization of MHBS, which constitutes another innovation. More details will be described in our contact model below.

2 Thermo-hydro-mechanical contact model of MH

2.1 Formation habits of MH

Santamarina and Ruppel (2010) have reported on different types of MH formation in MHBS. Figure 1 is a Scanning electron microscopy (SEM) image of MHBS, in

which MH forms between soil particles and bonds them together – cementation. Other forms of MH also exist such as pore-filling, particle coating and load bearing as illustrated in Figure 2 (Kumar Saw et al., 2013; Waite et al., 2009; Winters et al., 2004; Brugada et al., 2010; Dai et al., 2004). Experimental results of Masui et al. (2005) and Hyodo et al. (2007, 2013) show that the MH bonds play a pivotal role in the mechanical response of MHBS; hence we adopt a bond contact model in DEM analysis to capture the bulk strength and strain-softening response of MHBS with MH cementation.

2.2 Generalized force-displacement relationship and strength criterion of the contact model

The thermo-hydro-mechanical bond contact model originates from Jiang et al. (2014b), and has been advanced in this study. In this model, there are two situations of the bond contact, one when the particles are in contact and the other when the particles are not in contact (Figure 3). The overlap of a contact pair, u_n, could be expressed as:

$$u_n = r_1 + r_2 - d \tag{1}$$

where r_1 and r_2 are radii of the two particles and d is the distance between centers of the particles. Therefore, $u_n \geq 0$ refers to a contacted pair and $u_n < 0$ refers to non-contact pair in which the length of the bond if one exists is given by $l = -u_n$. The MH bonds are generated within particle pairs distanced less than a specific value, which we call critical distance l_{cr}. The critical length of the bond, l_{cr}, was based on the observations from SEM images of MHBS in previous laboratory

studies (Zhou, 2009). Seeking the largest gap of the MH bonds in the SEM images, the largest bond length was considered as the critical MH bond length. Zhou (2009) observed from the images that l_{cr} is affected by MH saturation. The relationship between critical MH bond length and MH saturation from Zhou (2009) is shown in Figure 4. After the non-bonded specimen has been created, MH bonds will form at contacts where $l < l_{\mathrm{cr}}$ (including those contacted particle pairs).

The force-displacement relationship of the model is applicable for both situations. This model considers the transmission of forces at contact as a combination of two parts: one is particle contact part and the other is MH bond part, which could be expressed as follows:

$$F_n = F_n^b + F_n^p \tag{2a}$$

$$F_s = F_s^b + F_s^p \tag{2b}$$

$$M = M^b + M^p \tag{2c}$$

where F_n, F_s and M are total normal force, shear force and moment transmitted at each particle contact, respectively; F_n^b, F_s^b and M^b are normal force, shear force and moment from MH bond part, respectively; F_n^p , F_s^p and M^p are those from particle contact part, respectively.

For particle contact part, when the two particles do not contact at MH formation, the forces, including normal force, shear force and moment, are all zero:

$$F_n^p = 0 , F_s^p = 0 , M^p = 0 \qquad u_n < 0 \tag{3}$$

when $u_n \geq 0$, the mechanical response could be written as follows, based on the rolling resistance model by Jiang et al. (2005). The shear force and bending moment

are incremental; that is to say, during each time step in calculation, they are refreshed by the former value added by incremental displacement/rotation multiplying corresponding stiffness.

$$F_n^p = k_n^p u_n \qquad u_n \geq 0 \tag{4a}$$

$$\begin{cases} F_s^p \leftarrow -k_s^p \Delta u_s^p + F_s^p \\ F_s^p \leq F_n^p \mu^p \end{cases} \qquad u_n \geq 0 \tag{4b}$$

$$\begin{cases} M^p \leftarrow -k_m^p \Delta\theta^p + M^p \\ M^p \leq F_n^p \beta^p r / 6 \end{cases} \qquad u_n \geq 0 \tag{4c}$$

where Δu_s^p , $\Delta\theta^p$ are the relative shear displacement and the relative rotation between the particles, respectively; k_n^p, k_s^p, k_m^p are the normal, shear and rotational stiffness, respectively; r is the average radius of the particles: $r = 2r_1 r_2 / (r_1 + r_2)$; μ^p is the friction coefficient between particles and β^p is the coefficient of rolling resistance as described in Jiang et al. (2005).

For the MH bond part, the mechanical response could be written as follows:

$$F_n^b = \begin{cases} k_n^b u_n^b & \text{not failure} \\ 0 & \text{failure} \end{cases} \tag{5a}$$

$$\begin{cases} F_s^b \leftarrow F_s^b + k_s^b u_s^b & \text{not failure} \\ F_{s(resid)}^b = \mu^b F_n^b & \text{failure} \end{cases} \tag{5b}$$

$$\begin{cases} M^b \leftarrow M^b + k_m^b \Delta\theta^b & \text{not failure} \\ M_{(\text{resid})}^b = F_n^b \beta^b r / 6 & \text{failure} \end{cases} \tag{5c}$$

where u_n^b is the compressive deformation of MH bond, which could be determined by the expression below:

$$u_n^b = u_n - u_{n0} \tag{5d}$$

u_{n0} is particle overlap when MH bond forms. Therefore, u_{n0} equals to u_n when a MH bond forms at an existing particle contact; if a MH bond forms between two particles not in contact (satisfying $l < l_{\mathrm{cr}}$), the u_{n0} is -1 times the particle gap. Δu_s^b and $\Delta\theta^b$ are the incremental shear displacement and rotation of the bond, respectively. The normal, shear and rotational bond stiffness, k_n^b, k_s^b and k_m^b, are all adopted from Jiang et al. (2014b) and shown below.

$$k_n^b = BE / l \tag{6a}$$

$$k_s^b = k_n^b / 1.5 \tag{6b}$$

$$k_m^b = k_n^b B^2 / 12 \tag{6c}$$

where E is the elasticity modulus of the MH bond and B is the width of MH bond, as shown in Figure 3. The stiffness ratio of MH bond could be derived from Poisson's ratio of MH. The stiffness ratio $\eta^b = \frac{k_n^b}{k_n^s} = \frac{\varepsilon_1^b}{\varepsilon_s^b}$, where ε_1^b and ε_s^b are axial and shear strain of MH, respectively. In addition, $\varepsilon_s^b = \varepsilon_1^b - \varepsilon_3^b = \varepsilon_1^b(1-\nu^b)$, in which ν^b is Poisson's ratio of MH. Then we can derive the relationship between η^b and ν^b as $\eta^b = \frac{\varepsilon_1^b}{\varepsilon_1^b(1-\nu^b)} = \frac{1}{1-\nu^b}$. Experimental data (Huo et al., 2011) show that the Poisson's ratio of MH is around 0.3. Adopting ν^b as 0.3, then $\eta^b = 1.43$. Thus we adopt stiffness ratio of MH bond as 1.5. μ^b is the sliding friction coefficient when MH bond is broken and $\beta^b = B / r$ is the rolling resistance coefficient of MH bond (Jiang et al., 2005). β^b, or B, is related to MH saturation S_{MH} (Jiang et al., 2014b):

$$S_{MH} = \frac{\sum_{i=1}^{n}[2\beta^b r^2 - 2r^2 \arcsin(\frac{\beta^b}{2}) - \beta^b r^2 \sqrt{1-\frac{\beta^{b2}}{4}}]}{V_v} + 26.4\% \tag{7}$$

where V_v is the total volume of voids in the MHBS.

There are two main criteria for MH bond failure: (a) tension / compression failure, when the normal force of an MH bond exceeds its tensile or compressive strength; (b) shear-moment failure, when the combined shear force and moment reaches the strength envelope of the bond, which is put forward by Jiang et al. (2012a, 2012b). The two criteria could be described in these expressions:

$$\begin{cases} -R_{tb} \le F_n^b \le R_{cb} & \text{not failure} \\ F_n^b < -R_{tb}, F_n^b > R_{cb} & \text{failure} \end{cases} \tag{8a}$$

$$\frac{F_s^2}{R_{sb}^2} + \frac{M^2}{R_{rb}^2} \begin{cases} <1 & \text{not failure} \\ =1 & \text{critical state} \\ >1 & \text{failure} \end{cases} \tag{8b}$$

where R_{tb}, R_{cb}, R_{sb} and R_{rb} are the tensile, compressive, shear and rotational resistance of the MH bond, respectively:

$$R_{tb} = B\sigma_{tMH} \tag{9a}$$

$$R_{cb} = B\sigma_{cMH} \tag{9b}$$

$$R_{sb} = \mu^b \cdot R_{cb} \cdot \frac{F_n^b + R_{tb}}{R_{cb} + R_{tb}} \cdot [1 + g_s (\ln \frac{R_{cb} + R_{tb}}{F_n^b + R_{tb}})^{f_s}] \tag{9c}$$

$$R_{rb} = \frac{r\beta^b R_{cb}}{6} \cdot \frac{F_n^b + R_{tb}}{R_{cb} + R_{tb}} \cdot [1 + g_r (\ln \frac{R_{cb} + R_{tb}}{F_n^b + R_{tb}})^{f_r}] \tag{9d}$$

where σ_{cMH}, σ_{tMH} are the compressive and tensile strength of pure MH bond respectively, which are related to temperature and water pressure and will be discussed further. Since there are few test results of resistance on MH bond, we have to seek some alternatives. Ice is considered very similar to MH in physical and

mechanical behavior (Dvorkin et al., 2003; Choi and Koh, 2009); moreover, comparison of strength envelope of Portland cement (Helmut et al., 1969; Hussein and Marzouk, 2000), resin (Ellyin and Xia, 2006) and ice (Nadreau and Michel, 1986) has shown that the strength envelope of ice is very close to that of Portland cement. Hence, we consider interpreting the resistance of MH bond by referring to the previous experimental results on Portland cement bond (Jiang et al., 2012a). Fitting the shear and rotational resistance envelope of the cement (Figures 5 and 6), it is found that the fitting function is as described in Eq. (9c) and (9d), respectively, with fitting parameters f_s, g_s, f_r, g_r that are related to the critical length of the bond, l_{cr}, which is the maximum gap between two particles where a MH bond will form. For gap larger than l_{cr}, MH bond will not form. The values of f_s, g_s, f_r, g_r are shown in Tables 1 and 2 with critical bond length 0.6mm, 1.0mm and 1.5mm, respectively. Then we can derive Eq. (10) by fitting f_s, g_s, f_r, g_r, which is shown in Figure 7.

$$f_s = 0.824 + 0.364\exp[-0.5(\frac{l_{\mathrm{cr}} - 1.069}{0.353})^2] \tag{10a}$$

$$g_s = 2.876 - 1.623\exp[-0.5(\frac{l_{\mathrm{cr}} - 1.236}{0.506})^2] \tag{10b}$$

$$f_r = 1/(2.719 - 3.207 l_{\mathrm{cr}} + 1.442 l_{\mathrm{cr}}^2) \tag{10c}$$

$$g_r = 3.068 l_{\mathrm{cr}}^2 - 7.347 l_{\mathrm{cr}} + 6.358) \tag{10d}$$

2.3 The effect of temperature and water pressure on mechanical behavior of MH

The Young's modulus (E) and the strength of MH bond (i.e., σ_{cMH} and σ_{tMH}) are influenced by temperature and water pressure, according to Hyodo et al. (2013). Thus this model consists of one unified temperature-water pressure parameter L, referring

to the minimum distance between the MH state point (the point with coordinates of temperature and water pressure in the phase equilibrium of MH (Sun et al., 2014)) and phase line. All the mechanical parameters of pure MH could be linked to parameter L to reflect the effect of both temperature and water pressure.

From experimental observations, they can be correlated to these environmental conditions and density as follows (Jiang et al., 2014b):

$$\frac{E}{p_a}=\begin{cases}7840L(T,\sigma_w)+8620\rho^*-4890 & L(T,\sigma_w)>0\\ 0 & L(T,\sigma_w)\le 0\end{cases} \tag{11a}$$

$$\frac{\sigma_{c,MH}}{p_a}=\begin{cases}715L(T,\sigma_w)+186\rho^*-133 & L(T,\sigma_w)>0\\ 0 & L(T,\sigma_w)\le 0\end{cases} \tag{11b}$$

$$\frac{\sigma_{t,MH}}{p_a}=\begin{cases}715L(T,\sigma_w-\sigma_{tMH})+186\rho^*-133 & L(T,\sigma_w-\sigma_{tMH})>0\\ 0 & L(T,\sigma_w-\sigma_{tMH})\le 0\end{cases} \tag{11c}$$

where σ_w is water pressure; T is temperature; ρ^* is the density of MH normalized by the density of water under 4°C and L is the minimum distance from the current thermo-hydro state point to the phase equilibrium line of MH.

The phase equilibrium of MH is shown as a relationship between temperature and water pressure in Figure 8, where the parameter L is the distance from the temperature-pressure state point to the MH phase line. There are several studies of the phase equilibrium line which are broadly in agreement (Sun et al., 2014; Chin et al., 2013; Hyodo et al., 2002). In this study, the line proposed by Hyodo et al. (2002) has been adopted. We can draw an expression of L by fitting to the data:

$$L(T,P)=\begin{cases}2-\sqrt{(T^*+0.9890)^2+(P^*-1.0711)^2} & \text{if (I)}\\ |11.9198T^*-P^*-11.0636|/11.9617 & \text{if (II)}\\ |426.7615T^*-P^*-484.9765|/426.7627 & \text{if (III)}\end{cases} \tag{12a}$$

$$\text{(I)}\ \begin{cases} 8.3894\times10^{-2}T^{*}+P^{*}-0.9881<0 \\ (T^{*}+0.9890)^{2}+(P^{*}-1.0711)^{2}<4 \end{cases} \tag{12b}$$

$$\text{(II)}\ \begin{cases} 8.3894\times10^{-2}T^{*}+P^{*}-0.9881>0 \\ 17.8560T^{*}+414.8010P^{*}-1079.5990<0 \\ 11.9189T^{*}-P^{*}-11.0636<0 \end{cases} \tag{12c}$$

$$\text{(III)}\ \begin{cases} 17.8560T^{*}+414.8010P^{*}-1079.5990>0 \\ 426.7615T^{*}-P^{*}-484.9765<0 \end{cases} \tag{12d}$$

where $T^{*}=T/243\text{K}$ and $P^{*}=P/1\text{MPa}$ refer to normalized temperature and water pressure respectively. Eq. (11) also indicates that the strength of MH bond increases with L that characterizes the combined effect of temperature and water pressure, which is one of the characteristics of the model.

3 DEM modeling of biaxial test and sample parameters

The thermo-hydro-mechanical bond contact model described above was used to simulate the biaxial tests of MHBS. The initial unbonded specimen with 24,000 particles was generated using the multi-layer compaction method proposed by Jiang et al. (2003). This achieves a homogeneous simulated specimen with an initial planar void ratio of 0.27 for the biaxial test simulation. A previous study has found that 6,000 particles are adequate to obtain a bulk behavior representation (Jiang et al., 2014b) whilst 24,000 particles were found to provide a good representation of strain localization phenomenon (Jiang et al., 2011, 2014a). Therefore, in this study we kept the number of particles at 24,000. The sample parameters are given in Table 3 and the DEM particle size distribution is shown in Figure 9. Such size distribution was kept the same as our previous studies (Jiang et al., 2005, 2014a, 2014b) for comparison.

The particle size adopted in this paper is 100 times larger than that in laboratory tests (Masui et al., 2005), in which the particle size ranged from 0.01-0.1mm. The scaling up of particle size has been shown to work whilst providing computational efficiency, as long as the number of particles is large enough to provide a stable bulk mechanical response (Jiang et al., 2014a, 2014b). All of the numerical MHBS specimens are given the same initial structure, with a maximum particle overlap of 2.3% of the average radius. The particle contact stiffness parameters, along with the particle friction coefficient, were adopted from the previous DEM study (Jiang et al., 2014a, 2014b). They are determined by trial-and-error and are chosen to match the mechanical behavior of the host sand in triaxial tests. The particle rolling resistance coefficient (relating to the irregularity of particle surface (Jiang et al., 2005)) is chosen as 0.5 through trial and error to match the bulk friction angle of MHBS as measured in the experiments (Zhang et al., 2012). The local damping was set at 0.7 which is the default value in PFC2D version 3.10 (Itasca, 2004). No viscous damping was needed since it was a quasi-static condition. The upper and lower boundaries for biaxial tests are two rigid walls and there is no friction between the rigid boundary and soil specimen. In this study, we adopt MH with density of 0.9g/cm^3 to match the experimental conditions (Hyodo et al., 2005). The MH rolling resistance coefficient β^b is assumed to be the same at all particle contacts and is related directly to the MH saturation (Eq. (7)), as long as the particle assembly is kept unchanged. For MH saturation of 50-55%, β^b is close to 1.0 in this study. Therefore, we adopt β^b=1.0 at all contacts for simplicity, giving a corresponding MH saturation of 53.2%. From

Figure 4, the critical distance l_{cr} is about 0.075 times the average particle size D_{50} (7.6mm). Thus l_{cr} could be calculated as 0.6mm which was adopted in this study.

We adopt flexible boundaries made up from grains at the side and colored the specimen in a mosaic style (Figure 10) to make shear band formation clear. After the confining pressure is balanced, the top boundary undergoes a 5%/min compression strain rate which is a quasi-static loading speed. The presence of a quasi-static regime could be determined as follows (O'Sullivan 2011):

$$\dot{\varepsilon}\sqrt{\frac{m}{p}} << 1 \tag{13}$$

where $\dot{\varepsilon}$ is strain rate, m is particle mass and p is confining pressure. In this study $\dot{\varepsilon}$ is 8.33×10^{-4} Hz, $m=\rho\frac{\pi D_{50}^2}{4}$=0.118kg, p=10^6 Pa. Then $\dot{\varepsilon}\sqrt{\frac{m}{p}} = 2.86\times10^{-7} << 1$. So this study is quasi-static. For quasi-static condition, the critical time increment dt_c can be calculated as follows:

$$dt_c = 2\pi\sqrt{\frac{m}{k}} \tag{14}$$

where k is particle normal contact stiffness and m is particle mass, respectively. In this study dt_c is calculated as 8.81×10^{-5}s. We usually use a time increment that is a fraction of dt_c, therefore the time increment of 10^{-5}s adopted in this study is appropriate. Measurement circles (a feature of PFC2D) are used to compute the macro and micro variables in the specimen.

4 Macro mechanical behavior of MHBS from DEM simulation

4.1 Effect of temperature on MHBS loading response

In this sub-section, we shall report on the biaxial test simulations of MHBS at three different temperatures: 274K, 278K and 283K respectively (T^*=1.128, 1.144 and 1.165 respectively) whilst keeping the water pressure and the effective confining pressure constant at 10MPa and 1MPa respectively. The temperatures chosen in this study were representative temperature of MH formation and adopted by previous MHBS experiments (Hyodo et al., 2013). Figure 11 presents the deviatoric stress-axial strain relationship as well as the volumetric strain-axial strain relationship. Figure 11 shows that after peak failure, the MHBS shows characteristic of strain-softening, with the deformation resulting in dilatancy and shear band formation. This result is in agreement with experimental observations by Masui et al. (2005), in which MHBS shows vast strain-softening as MH saturation 55.1% that is close to 53.2% in this study. Although the post-peak stress in our study goes down more rapidly that Masui et al. (2005), a qualitative agreement exists. As temperature increases, the peak deviatoric stress decreases. That is because the parameter L decreases with increasing temperature at a constant water pressure, leading to weakened strength of MH bond. However, the volume increase (dilatancy) after the peak failure that is associated with the shear band formation does not appear to follow any particular trend with increasing temperature. Further investigation reveals that this is due to different shear band modes. Samples for 274K and 278K produce localized shear bands which initiate at the bottom specimen boundary whereas the sample at 283K has localized

shear band at the mid height of the sample (away from both top and bottom boundaries). The different shear band locations will be discussed later considering all 60 simulations presented in this paper. What is clear is that volumetric change post peak failure is sensitive to the location of the shear band in the sample.

Figure 12 shows the predicted strength envelope of the MHBS specimens at the three temperatures. The simulations were performed at effective confining pressure of 0.5MPa, 1MPa and 2MPa, which are close to the stress levels experienced by MHBS in a deep seabed. The predicted cohesion at peak state, the peak friction angle and the residual friction angle are summarised in Table 4. Both the peak strength and the residual strength of MHBS decrease with increasing temperature. In addition, MHBS exhibits a significant cohesion value at peak state but no cohesion at residual state; and a lower friction angle at peak state than at residual state. In other words, the existence of MH bonds will increase the bulk cohesion while decreasing the friction angle of the MHBS. This finding from the DEM model corroborates with the laboratory observations on MHBS (Zhang et al., 2012). In addition, results of Zhang et al. (2012) show cohesion and friction angle of MHBS 1.16MPa and 12.4° , respectively, as MH saturation is 48.9%~51.3%, which is closest to that in this study. The data in Tables 4 and 5 correspond to such result, showing the efficiency of discrete element simulation in reflecting bulk behavior of MHBS.

4.2 Mechanical behavior of MHBS under different water pressures

In this sub-section, we shall present specimens with MH at three different water

pressures: 5MPa, 10MPa and 20MPa while keeping the temperature at 274K and the effective confining pressure at 1MPa. The deviatoric stress-axial strain relationship as well as the volumetric strain-axial strain relationship is shown in Figure 13. As water pressure increases, the peak stress of MHBS increases due to the increase of the parameter L and hence the increase of MH bond strength. Significant dilatancy is predicted to occur immediately after reaching the peak strength which is associated with the shear band formation. The overall dilatancy appears to be similar for the two specimens at 10MPa and 20MPa but noticeably smaller when the water pressure is the lowest at 5MPa, for less MH bonds break finally as water pressure increases.

Figure 14 shows the strength envelope of MHBS specimens at the three water pressures. The specimens are tested with effective confining pressure 0.5MPa, 1MPa and 2MPa, respectively, just the same as testing of MHBS at different temperatures. The computed cohesion at peak state, the peak friction angle and the residual friction angle are shown in Table 5. Both the peak friction angle and the residual friction angle increase with water pressure. Again, the MHBS exhibits a significant cohesion value at peak state but no cohesion at residual state.

5 Strain localization of MHBS at varying temperature and water pressure

The results above show that the strength of MHBS increases with increasing water pressure and decreasing temperature, which is the result of the change in the micro MH bond strength with temperature and water pressure. To study the micro-mechanical phenomena, we focus on three temperature-water pressure

conditions in this section: (a) T=274K, σ_w=5MPa; (b) T=274K, σ_w=10MPa; (c) T=283MPa, σ_w=10MPa. The comparison of (a) and (b) refers to the effect of increased water pressure, while the comparison of (b) and (c) reflects the effect of increased temperature. The effective confining pressures all remain at 1MPa.

5.1 Deformation pattern

The stress-strain response of MHBS is shown at six stages which are marked in Figures 11(a) and 13(a) with points O-E, which refer to starting point (O), initial yield point (A), peak stress point (B), strain-softening point (C), steady point (D) and end point of simulation (E), respectively. Figure 15 provides the deformation patterns of the three specimens mentioned in last sub-section at the six points under the effective confining pressure of 1MPa. The results show that shear band appears after peak stress is reached (point B) and becomes more distinct as axial strain increases. It is interesting is that as temperature and water pressure change, different types of shear band appear. To shed light on this occurrence, a total of 60 biaxial tests are simulated under different temperature and water pressure conditions while keeping the same effective confining pressure of 1MPa. The temperature-water pressure combinations explored and the resulting type of shear band in each simulation are shown in Figure 16. The three types of shear band have been depicted in Figure 15 above. These shear band formations arise from the microscopic phenomena which will be discussed further below.

5.2 Bond breakage fields and rates

It is known that strain localization of MHBS is deeply related to its bond breakage, according to Jiang et al. (2014a). The bond breakage field of MHBS with three different temperature-water pressure conditions is shown in Figure 17. It is observed that there is little bond breakage before peak stress (point A). At the peak stress (point B), the criss-cross pattern of shear band is starting to emerge throughout the specimen before developing into a distinct concentrated shear band where the bond breakages concentrate largely in the shear band (point C). The result is in corroboration with previous studies (Jiang et al., 2013, 2014a), reflecting that strain localization of MHBS is related to bond breakage in the specimens.

Figure 18 shows the rate of bond breakage of the three MHBS specimens. The rate of bond breakage $\dot{N}$ could be described as:

$$\dot{N} = \frac{\Delta N}{\Delta \varepsilon_1} \tag{13}$$

where ε_1 is axial strain and N is the number of broken bonds. The stress-strain relationships are also plotted for comparison. The bond breakage rate reaches maximum just before the peak deviatoric stress and stays at a high breakage rate before dropping off as peak state is reached. The bond breakage evolution is close to that of stress-strain relationship, which is similar to Jiang et al. (2014a).

In section 2, we have discussed the two criteria of failure of MH bond: tension/compression failure and shear-moment failure. The combination of these criteria may lead to four types of bond failure: tension failure, compression failure,

shear-moment failure where the bond is in tension and shear-moment failure where the bond is in compression. Figure 19 shows the build-up of the four bond breakage modes during the axial loading of MHBS specimens at the three temperature-water pressure conditions. Under 274K/5MPa and 274K/10MPa, bond failures are mostly in the shear-moment mode in tension, whilst under 283K/10MPa, bonds fail mainly in simple compression. Looking into the result of different types of shear band, we observe predominant bond failures in shear-moment whilst in tension form shear band Type 1 and 2 and predominant bond failures in compression form shear band Type 3. Furthermore, it is noted in Figure 16 that when the temperature increases beyond 281K, the MHBS becomes more unstable which tends to result in Type 3 type failure in biaxial loading. To the left side of the dashed line where MH is stable and MH bond is stronger, Types 1 or 2 shear band modes prevail. Therefore, it is probable that different types of bond breakage lead to different types of shear band. In addition, Type 3 shear band is at the middle of the specimen, while Types 1 and 2 both hit the lower boundary. Thus, the bond breakage type may have an impact on position of shear band.

5.3 Contact force chains, principal stress fields, particle velocity fields, and APR distributions

Figure 20 presents the evolution of contact force chains, principal stress, particle velocity and average pure rotation (APR) of the MHBS simulations at the three temperature and water pressure conditions. They are depicted at the six points of O to E as in Figures 11 and 13.

Force chain is shown by representing each normal contact force with a line connecting the centers of the two contacted granules with the line thickness representing the magnitude of the force. Denser force chains mean stronger particle contact forces. In addition, blue force chains refer to compressive contact forces and red chains are tensile. From the figure we can find that after peak stress and shear band appearance, the force chains become more and more concentrated due to the masses of bond breakage and the re-distribution of contact forces, which is in corroboration with the stress field below; at the same time, regions with very few and weak force chains emerge. Such phenomenon is not so obvious in the specimen with temperature of 274K and stress of 5MPa due to the effects of lower boundary on granular contact forces at the shear bands.

The stress field is computed at many positions in the specimen using measurement circle with a radius of 0.08m and calculating the principal stress at the center of each measurement circle. The longer line of the cross refers to the major principal stress and the shorter line refers to the minor principal stress. The direction of each line refers to the direction of the stress while the length refers to the magnitude. From the figure we can find that after peak stress, the principal stress at the position of shear band starts to rotate while that outside shear band keeps unchanged. This result is in corroboration with previous studies (Jiang et al., 2011, 2014a). The major principal stress rotates corresponding to the force chain, reflecting the relationship between macro and micro mechanical responses of MHBS.

The velocity field is conducted by calculating velocities of all particles (velocity is

obtained by particle displacement over time period) and drawing a line of each particle with a proper length to represent the value of velocity. Larger length means higher velocity of the particle. This method has been adopted in virtualization of previous DEM studies (Jiang et al., 2006; Chin et al., 2013). From the figure we can find that after peak stress, the particles at shear bands start to move outwards to the shear band, leaving the velocity field blank at the position of the shear band. This result correlates with previous study (Jiang et al., 2014a). As temperature increases or water pressure decreases, the area of the blank increases due to the decrease of strength of MH bond and more particles spreading out after bond breakage.

Now let's turn to particle rotation. The average pure rotation rate (APR) is put forward by Jiang et al. (2005) and could be used as one of the kinematic characteristics of granules during loading. The APR in each measurement circle is calculated as follows:

$$\omega = \frac{1}{N}\sum_{k=1}^{N}\left[\frac{\dot{\theta}_1^{(k)} r_1^{(k)} + \dot{\theta}_2^{(k)} r_2^{(k)}}{r^{(k)}}\right] \tag{14}$$

where ω is APR, N is number of particle contacts, $r^{(k)}$ is the average radius of the two contacted particles at each contact, $r_1^{(k)}$ and $r_2^{(k)}$ are radii of the two particles at each contact, respectively and $\dot{\theta}_1^{(k)}$ and $\dot{\theta}_2^{(k)}$ are the pure rotation rates of the two particles at each contact. Then a contour of the APR is shown. From the figure we can find that after peak stress, the APR tends to concentrate within the shear band regions, which corroborates with previous study (Jiang et al., 2014a). It is noted that in the specimen 274K/5MPa, the APRs in the two shear bands have different colors. That is because the particles at the two regions have opposite rotational directions. As

temperature increases or water pressure decreases, the area with significant changes in APR increases due to the increasing instability of MH bonds.

All the micro variables above have shown the micro characteristics of MHBS during strain localization. That is, the strain localization of MHBS is accompanied by localization of all the micro valuables of MHBS, and such localization turns more obvious as temperature and water pressure conditions weaken the MH bonds.

5.4 Evolution of void ratio and pure rotation value inside and outside of a shear band

Here, we explore the difference of macro and micro variables inside and outside of a shear band. Figure 21 shows the measurement circles set inside and outside the shear band of each of the three specimens described above. The measurement circles in the shear band are marked 1 to 3 while those outside the shear band are marked 5 to 8. Figure 22 shows the relationships of the void ratio and the pure rotation value with the axial strain for the three MHBS specimens. The pure rotation value is the time integral of APR in each measurement circle:

$$\Omega_0 = \int_0^{t_0} \omega dt = \sum_{i=1}^{n} \omega^i \Delta t \text{ (if } \Delta t \text{ is small and } \Delta t = \frac{t_0}{n}) \tag{15}$$

where Ω_0 is pure rotation value at time t_0, ω^i is APR at time t_i, Δt is incremental time and n is an integer, respectively. The legend of the figure shows the number of the measurement circle. It is evident that before peak stress (point B), both void ratio and pure rotation value are largely similar and follow similar trends irrespective of the measurement positions; however, after peak stress and shear band

appearance, the void ratio inside the shear band starts to increase rapidly (dilation) before decreasing over further axial straining with intermittent sharp changes arising from local failure events. It is noted that the increase of void ratio within the shear band is very rapid for the 274K/5MPa case, which becomes less so when the stress level increases to 10MPa and more rapid again for the 283K/10MPa case. This is because the 274K/10MPa is the most stable condition where lighter bond breakage and inflation happen, compared to other conditions. Outside the shear band, the void ratio typically increases slightly immediately after reaching peak state and stays largely constant thereafter. Within the shear band, the pure rotation value increases (or decreases depending on the direction of the shear band) continually during the axial straining but remains largely constant outside the shear band. These observations are in corroboration with the previously reported study (Jiang et al., 2014a).

5.5 Geometric characteristics of shear bands of MHBS

The thickness and inclination angle of shear band are two main aspects in analyzing the progressive failure, as proposed in Jiang et al. (2014a). Figures 15, 17 and 20 can all be used to evaluate the thickness and inclination angle. In this study, we adopt the deformation pattern, the stress field, the distributions of bond breakage and APR distribution as evaluation criteria following the methodologies adopted in Jiang et al. (2011, 2014a). The MHBS specimens at post peak points C, D and E are evaluated.

Table 6 (a) and (b) show the thickness and inclination angle of shear band in the three MHBS specimens, respectively. For the 274K/5MPa specimen, the two shear

bands are evaluated separately. The results show that (1) as axial strain increases, the thickness of shear band increases gradually, while the inclination angle remains stable; (2) the average thickness of shear band is 9-20 times the average particle dimension, which is in corroboration with Jiang et al. (2013b); the average inclination angle of shear band is in the range of 47°-51°; (3) as temperature increases or water pressure decreases, both the thickness and inclination angle of shear band increase.

6 Conclusion

This study presents a DEM study of the mechanical behavior and strain localization of methane hydrate bearing sediments (MHBS) at different temperatures and water pressures. A thermo-hydro-mechanical contact model of MHBS has been adopted in simulations of several biaxial tests in which the mechanical behavior of MHBS under the influence of temperature and water pressure has been studied. Three simulated MHBS specimens at different temperature-water pressure conditions have been investigated thoroughly to provide insights on the evolution of the macro and micro variables, including deformation patterns, bond breakage rate and field, principal stress fields, contact force chains, particle velocity fields and APR distributions, during the strain localization of MHBS. Geometric characteristics of shear band have also been studied. The results show that:

(1) MHBS exhibits a peak strength followed by strain-softening with dilatancy concentrated in the shear band. The existence of MH increases the cohesion but decreases the friction angle of MHBS, which is in corroboration with previous study

(Zhang et al., 2012). As temperature increases or water pressure decreases, both the cohesion and friction angle of MHBS decrease but dilatancy increases, as a result of weaker MH bonds.

(2) Shear band develops largely after the peak stress with the great majority of bond breakage occurring in the region of shear band. The relationship between bond breakage rate and axial strain follows the trend of the stress-strain relationship. Other micro and macro variables such as contact force chains, principal stress fields, particle velocity fields and APR distributions are also localized during strain localization. Though temperature and water pressure change, the appearance of localization of these variables still remains similar. These results are in corroboration with previous study (Jiang et al., 2014a).

(3) Three different forms of shear band emerge as temperature and water pressure changes. Moreover, a new insight has been made about strain localization of MHBS that this phenomenon probably results from different types of bond breakage as the temperature-water pressure condition of MH is not so stable (the state point of MH is close to the equilibrium line) where the position of shear band is at the central specimen, while shear band occurs at the boundary when MH is relatively stable, in which bond breakage differs.

(4) As temperature increases or water pressure decreases, both the thickness and inclination angle of shear band increase.

Acknowledgements

This work is funded by China National Funds for Distinguished Young Scientists (No. 51025932). Funding by State Key Laboratory of Disaster Reduction in Civil Engineering, Tongji University (No. SLDRCE14-A-04) is also acknowledged.

References

Brugada, J., Cheng, Y.P., Soga, K., 2010. Discrete element modeling of geomechanical behavior of methane hydrate soils with pore-filling hydrate distribution. Granul. Matter 12, 517-525.

Chin, H.Y., Lee, B.S., Chen, Y.P., Chen, P.C., Lin, S.T., Chen, L.J., 2013. Prediction of phase equilibrium of methane hydrates in the presence of ionic liquids. Ind. Eng. Chem. Res. 52, 16985-16992.

Choi, J.H., Koh, B.H., 2009. Compressive strength of ice-powder pellets as portable media of gas hydrate. Int. J. Precis. Eng. Man. 10: 85-88.

Chung, Y.-C., Ooi, J.Y., 2008. Study of influence of gravity on bulk behaviour of particulate solid. Particuology. 6, 467-474.

Cundall, P.A., Strack, O.D.L., 1979. A discrete numerical model for granular assemblies. Geotechnique. 29, 47-65.

Dai, J., Xu, H., Snyder, F., Dutta, N., 2004. Detection and estimation of gas hydrates using rock physics and seismic inversion: Examples from the northern deepwater Gulf of Mexico. The Leading Edge 23, 60-66.

Dvorkin, J., Helgerud, M.B., Waite, W.F., Kirby, S.H., Nur, A., 2003. Introduction to physical properties and elasticity models, in: Natural Gas Hydrate, Springer Netherlands, pp. 245-260.

Ellyin, F., Xia, Z., 2006. Nonlinear viscoelastic constitutive model for thermoset polymers. J. Eng. Mater. T. 128: 579-585.

Evans, D., King, E.L., Kenyon, N.H., Brett, C., Wallis, D., 1996. Evidence for long-term instability in Storegga region off western Norway. Mar. Geol. 130, 281-292.

Freij-Ayoub, R., Tan, C., Clennell, B., Tohidi, B., Yang, J., 2007. A wellbore stability model for hydrate bearing sediments. J. Petrol. Sci. Eng. 57, 209-220.

Holtzman, R., 2009. Mechanical properties of granular materials: A variational approach to grain-scale simulations. Int. J. Numer. Anal. Met. 33, 391-404.

Huo, H., Liu, Y., Zheng, Z.Y., Zhao, J.J., Jin, C.Q., Lv, T.Q., 2011. Mechanical and thermal properties of methane clathrate hydrates as an alternative energy resource. J. Renew. Sustain. Ener. 3, 063110.

Hussein, A., Marzouk, H., 2000. Behavior of high-strength concrete under biaxial stresses. ACI Mater. J. 97: 27-36.

Hyodo, M., Hyde, A.F.L., Nakata, Y., Yoshimoto, N., Fukunaga, M., Kubo, K., Nanjo, Y., Matsuo, T., Nakamura, K., 2002. Triaxial compressive strength of methane hydrate, in: Chung, J.S., Sayed, M., Kashiwagi, M., Setoguchi, T., Hong, S.W. (Eds.), International Offshore and Polar Engineering Conference Proceedings. International Society Offshore & Polar Engineers, Cupertino, pp. 422-428.

Hyodo, M., Nakata, Y., Yoshimoto, N., Yoneda, J., 2007. Mechanical behavior of

methane hydrate-supported sand, in: International Symposium on Geotechnical Engineering Ground Improvement and Geosynthetics for Human Security and Environmental Preservation. Thai Contractors, Bangkok, pp. 195-208.

Hyodo, M., Yoneda, J., Yoshimoto, N., Nakata, Y., 2013. Mechanical and dissociation properties of methane hydrate-bearing sand in deep seabed. Soils. Found. 53, 299-314.

Itasca Consulting Group, 2004. PFC Manual, version 3.10.

Jiang, M.J., Konrad, J.M., Leroueil, S., 2003. An efficient technique for generating homogeneous specimens for DEM studies. Comput. Geotech. 30, 579-597.

Jiang, M.J., Leroueil, S., Konrad, J.M., 2004. Insight into shear strength functions of unsaturated granulates by DEM analyses. Comput. Geotech. 31, 473-489.

Jiang, M.J., Yu, H.-S., Harris, D., 2005. A novel discrete model for granular material incorporating rolling resistance. Comput. Geotech. 32, 340-357.

Jiang, M.J., Yu, H.S., Harris, D., 2006. Discrete element modelling of deep penetration in granular soils. Int. J. Numer. Anal. Met. 30, 335-361.

Jiang, M.J., Zhu, H.H., Li, X.M., 2010. Strain localization analyses of idealized sands in biaxial tests by distinct element method. Front. Earth. Sci. China. 4, 208-222.

Jiang, M.J., Yan, H.B., Zhu, H.H., Utili, S., 2011. Modeling shear behavior and strain localization in cemented sands by two-dimensional distinct element method analyses. Comput. Geotech. 38, 14-29.

Jiang, M.J., Sun, Y.G., Xiao, Y., 2012a. An experimental investigation on the mechanical behavior between cemented granules. Geotech. Test. J. 35, 678-690.

Jiang, M.J., Sun, Y.G., Li, L.Q., Zhu, H.H., 2012b. Contact behavior of idealized granules bonded in two different interparticle distances: An experimental investigation. Mech. Mater. 55, 1-15.

Jiang, M.J., Shen, Z.F., Thornton, C., 2013a. Microscopic contact model of lunar regolith for high efficiency discrete element analyses. Comput. Geotech. 54, 104-116.

Jiang, M.J., Zhang, W.C., Sun, Y.G., Utili, S., 2013b. An investigation on loose cemented granular materials via DEM analysis. Granul. Matter 15, 65-84.

Jiang, M.J., Sun, Y.G., Yang, Q.J., 2013c. A simple distinct element modeling of the mechanical behavior of methane hydrate bearing sediments in deep seabed. Granul. Matter 15, 209-220.

Jiang, M.J., Chen, H., Tapias, M., Arroyo, M., Fang, R., 2014a. Study of mechanical behavior and strain localization of methane hydrate bearing sediments with different saturations by a new DEM model. Comput. Geotech. 57, 122-138.

Jiang, M.J., Zhu, F.Y., Liu, F., Utili, S., 2014b. A bond contact model for methane hydrate bearing sediments with interparticle cementation. Int. J. Numer. Anal. Met. 38, 1823-1854.

Jiang, M.J., Zhang, F.G., Sun, Y.G., 2014c. An evaluation on the degradation evolutions in three constitutive models for bonded geomaterials by DEM analyses. Comput. Geotech. 57, 1-16.

Jiang, M.J., Dai, Y.S., Cui, L., Shen, Z.F., Wang, X.X., 2014d. Investigating mechanism of inclined CPT in granular ground using DEM. Granul. Matter 16, 785-796.

Jiang, M.J., Liu, F., Shen, Z.F., Zheng, M., 2014e. Distinct element simulation of lugged wheel performance under extraterrestrial environmental effects. Acta Astronaut. 99, 37-51.

Jiang, M.J., Zhu, F.Y., Utili, S., 2015a. Investigation into the effect of backpressure on the mechanical behavior of methane-hydrate-bearing sediments via DEM analyses. Comput. Geotech. 69, 551-563.

Jiang, M.J., Zhang, W.C., 2015b. DEM analyses of shear band in granular materials. Eng. Computation. 32, 985-1005.

Jiang M.J., Sun, C., Crosta, G.B., Zhang, W.C., 2015c. A study of submarine steep slope failures triggered by thermal dissociation of methane hydrates using a coupled CFD-DEM approach. Eng. Geol. 190, 1-16.

Jung, J.W., Santamarina, J.C., Soga, K., 2012. Stress-strain response of hydrate-bearing sands: Numerical study using discrete element method simulations. J. Geophys. Res. Solid Earth 117, B04202.

Kataoka, S., Yamashita, S., Suzuki, T., Nishio, S., 2008. Soils properties of the shallow type methane hydrate-bearing sediments in the Lake Baikal, in: Burns, S.E., Mayne, P.W., Santamarina, J.C. (Eds.), Deformation Characteristics of Geomaterials, Vols. 1 and 2. IOS Press, Amsterdam, pp. 299-302.

Kreiter, S., Feeser, V., Kreiter, M., Morz, T., Grupe, B., 2007. A distinct element simulation including surface tension-towards the modeling of gas hydrate behavior. Comput. Geosci. 11, 117-129.

Kupfer, H., Hilsdorf, H.K., Rusch, H., 1969. Behavior of concrete under biaxial

stresses, in: ACI Journal proceedings (Vol. 66, No. 8), ACI, Farmington Hills, pp. 656-666.

Li, Y., Zhao, H., Yu, F., Song, Y., Liu, W., Li, Q., Yao, H., 2012. Investigation of the Stress–Strain and Strength Behaviors of Ice Containing Methane Hydrate. J. Cold Reg. Eng., 26(4), 149-159.

Masui, A., Haneda, H., Ogata, Y., Aoki, K., 2005. Effects of methane hydrate formation on shear strength of synthetic methane hydrate sediments, in: Chung, J.S., Hong, S.W., Koo, J., Komai, T., Koterayama, W. (Eds.), Proceedings of the Fifteenth (2005) International Offshore and Polar Engineering Conference, Vol. 1. International Society Offshore & Polar Engineers, Cupertino, pp. 364-369.

Nadreau, J.P., Michel, B., 1986. Yield and failure envelope for ice under multiaxial compressive stresses. Cold Reg. Sci. Technol. 13: 75-82.

Ng, M.Y.A., Klar, A., Soga, K., 2008. Coupled soil deformation-flow-thermal analysis of methane production in layered methane hydrate soils, in: Offshore Technology Conference, DOI: 10.4043/19364-MS.

O'Sullivan, 2011. Particulate discrete element modelling. Spon Press, London and New York.

Santamarina, J.C., Ruppel, C., 2010. The impact of hydrate saturation on the mechanical, electrical, and thermal properties of hydrate-bearing sand, silts, and clay. Geophysical Characterization of Gas Hydrates, Geophys. Dev. Ser. 14, 373-384.

Saw, V.K., Udayabhanu, G.N., Mandal, A., Laik, S., 2013. Methane hydrate formation and dissociation in the presence of bentonite clay suspension. Chem. Eng. Technol. 36,

810-818.

Stegmann, T., Török, J., Brendel, L., Wolf, D.E., 2011. Minimal dissipation theory and shear bands in biaxial tests. Granul. Matter 13, 565-572.

Sun, S.C., Liu, C.L., Ye, Y.G., Liu, Y.F., 2014. Phase behavior of methane hydrate in silica sand. J. Chem. Thermodyn. 69, 118-124.

Uchida, S., Soga, K., Yamamoto, K., 2012. Critical state soil constitutive model for methane hydrate soil. J. Geophys. Res. 117, B03209.

Waite, W.F., Shin, H., Soga, K., Winters, W.J., Yun, T.S., Santamarina, J.C., Cortes, D.D., Dugan, B., Espinoza, D.N., Germaine, J., Jang, J., Jung, J.W., Kneafsey, T.J., 2009. Physical properties of hydrate-bearing sediments. Rev. Geophys. 47, 38.

Wang, S.Y., Zheng, W., Lu, X.B., Li, Q.P., 2009. The effects of gas hydrate dissociation on the stability of pipeline in seabed, in: Chung, J.S., Prinsenberg, S., Hong, S.W., Nagata, S. (Eds.), Proceedings of the Nineteenth (2009) International Offshore and Polar Engineering Conference. International Society of Offshore and Polar Engineers, Cupertino, pp. 49-53.

Wang, Y.H., Leung, S.C., 2008. Characterization of cemented sand by experimental and numerical investigations. J. Geotech. Geoenviron. 134, 992-1004.

Winters, W.J., Pecher, I.A., Waite, W.F., Mason, D.H., 2004. Physical properties and rock physics models of sediment containing natural and laboratory-formed methane gas hydrate. Am. Mineral. 89, 1221-1227.

Yan, R.-T., Wei, C.-F., Wei, H.-Z., Tian, H.-H., Wu, E.-L., 2013. A generalized critical state model for gas hydrate-bearing sediments, in: Yang, Q., Zhang, J.-M., Zheng, H.,

Yao, Y.P. (Eds.), Constitutive Modeling of Geomaterials: Advances and New Applications. Springer Berlin Heidelberg, Berlin ,pp. 649-656.

Yoneda, J., Hyodo, M., Nakata, Y., Yoshimoto, N., Imamura, Y., Tenma. N., 2011. Localized deformation of methane hydrate-bearing sand by plane strain shear tests, in: Proceedings of the 7th International Conference on Gas Hydrates, Edinburgh, Scotland, United Kingdom, July 17-21.

Yu, Y., Cheng, Y.P., Soga, K., 2012. Mechanical behaviour of methane hydrate soil sediments using discrete element method: Pore-filling hydrate distribution, in: Wu, C.-Y. (Eds.), Discrete Element Modelling of Particulate Media. RSC Publishing, London, pp. 264-270.

Zhang, X.-H., Lu, X.-B., Zhang, L.-M., Wang, S.-Y., Li, Q.-P., 2012. Experimental study on mechanical properties of methane-hydrate-bearing sediments. Acta Mech. Sinica. 28, 1356-1366.

Zhou, C., Ooi, J.Y., 2009. Numerical investigation of progressive development of granular pile with spherical and non-spherical particles. Mech. Mater. 41, 707-714.

Zhou, Y.P., 2009. Experiments on the inter-particle contact law of methane hydrate bearing soils and DEM analysis of their bearing capacity. Tongji University, Shanghai.

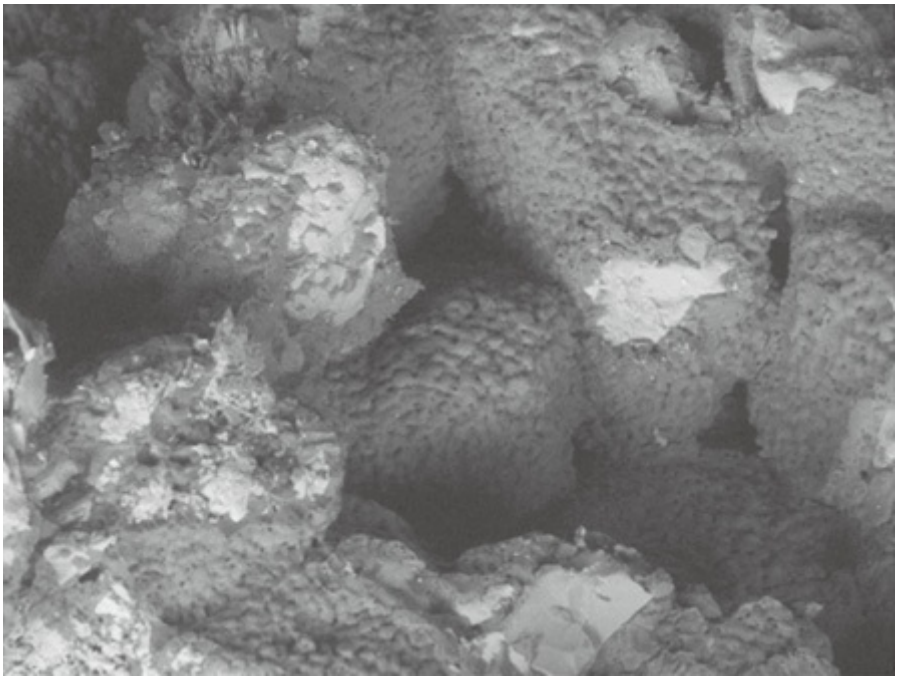

Figure 1. SEM image of MHBS (Saw et al., 2013).

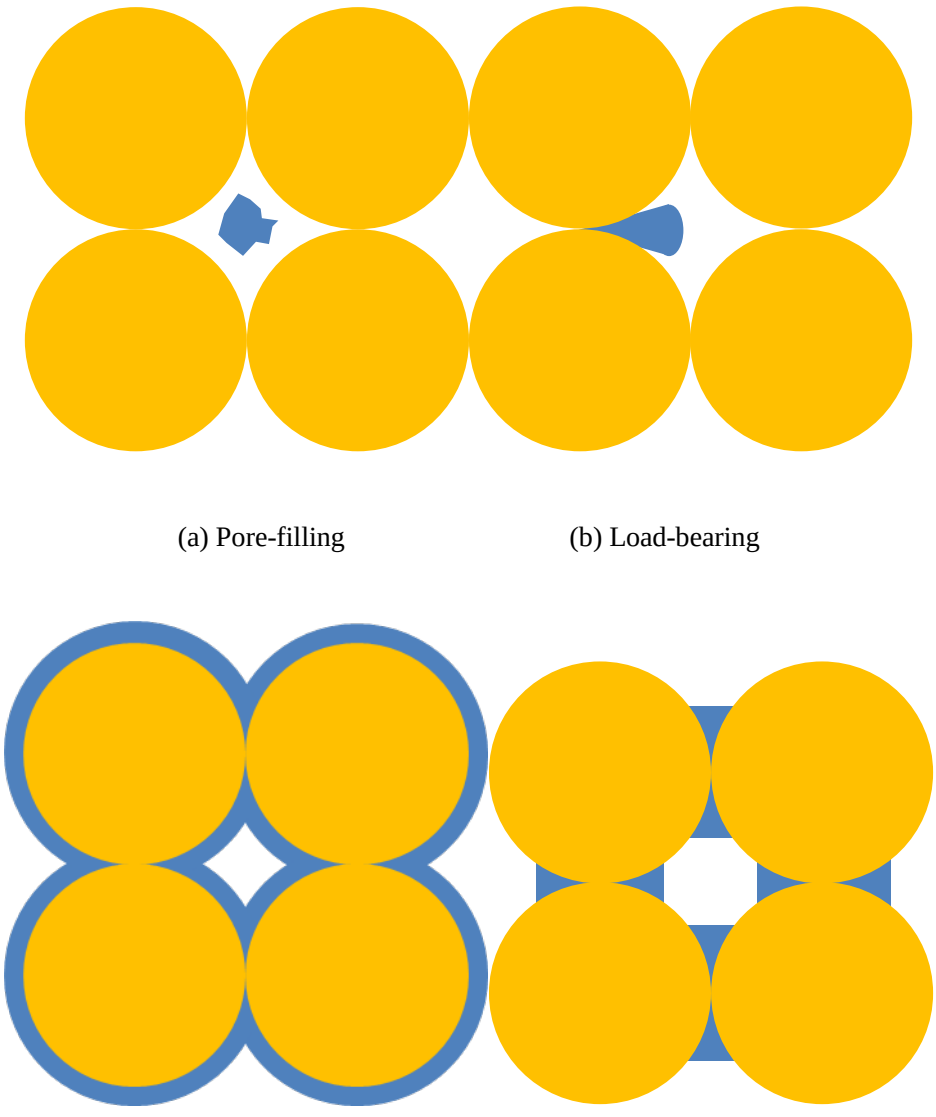

(a) Pore-filling (b) Load-bearing

(c) Coating (d) Cementation

Figure 2. Formation habits of MH.

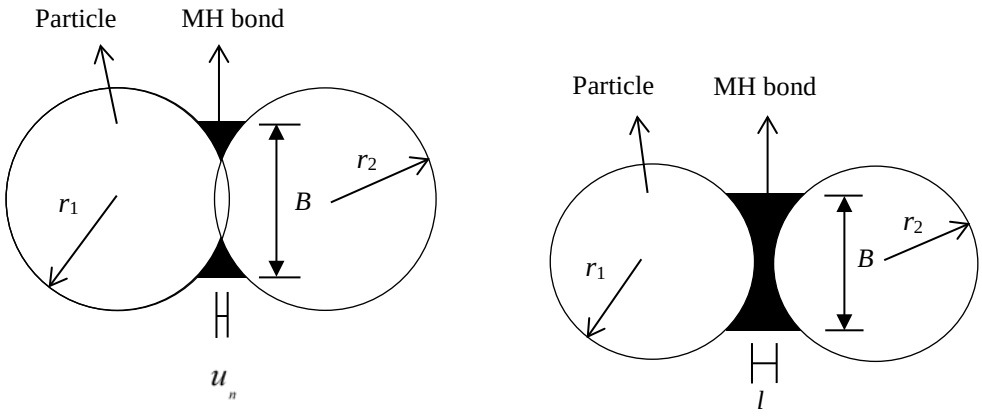

(a) Particles in contact (b) Particles not in contact

Figure 3. Illustration of MH bond contact model.

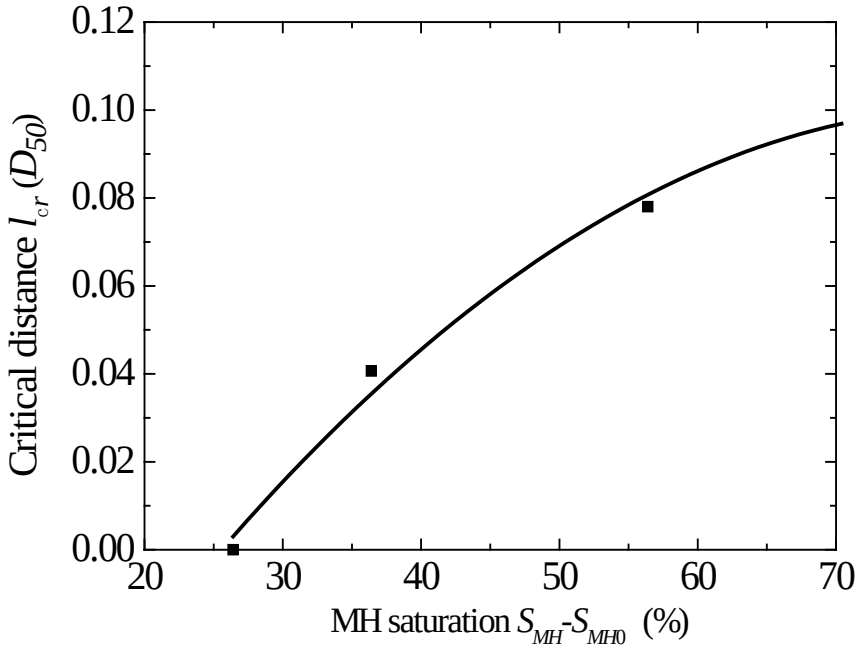

Figure 4. Relationship between critical MH bond length and MH saturation (Zhou, 2009).

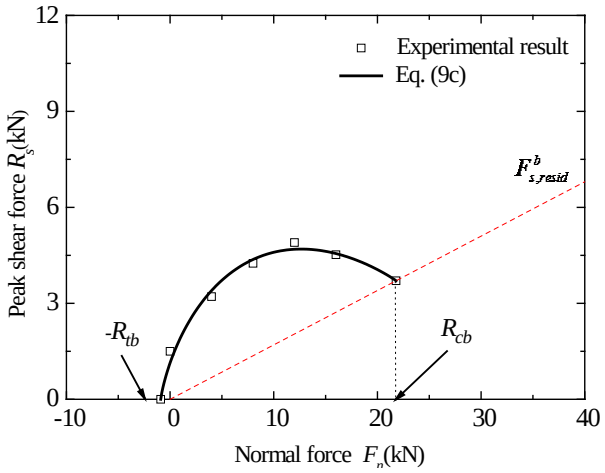

(a) Critical bond length 0.6mm

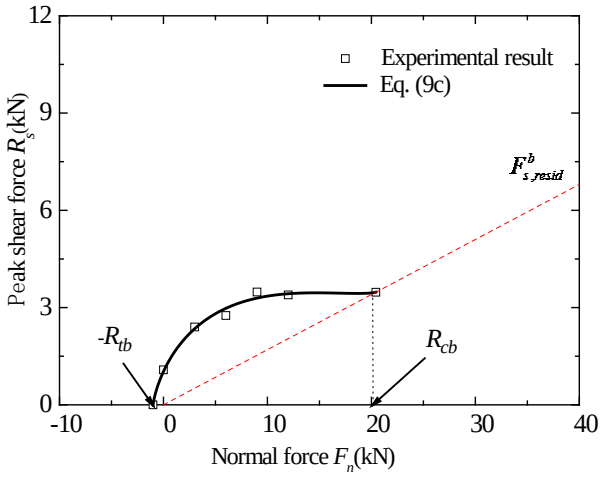

(b) Critical bond length 1.0mm

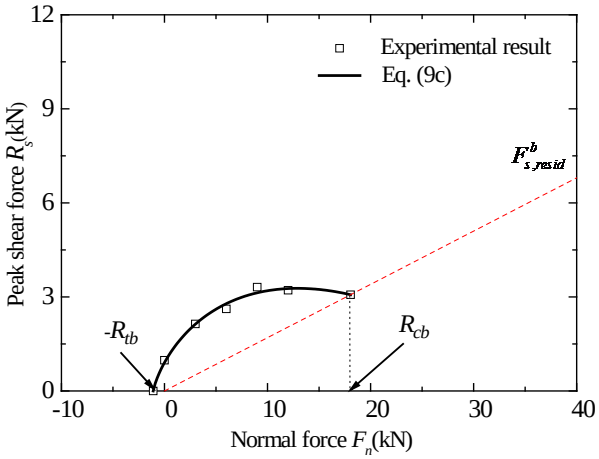

(c) Critical bond length 1.5mm

Figure 5. Shear strength envelope of cement bond.

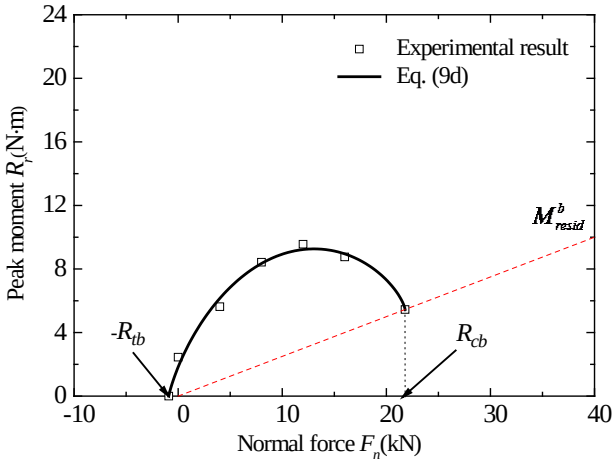

(a) Critical bond length 0.6mm

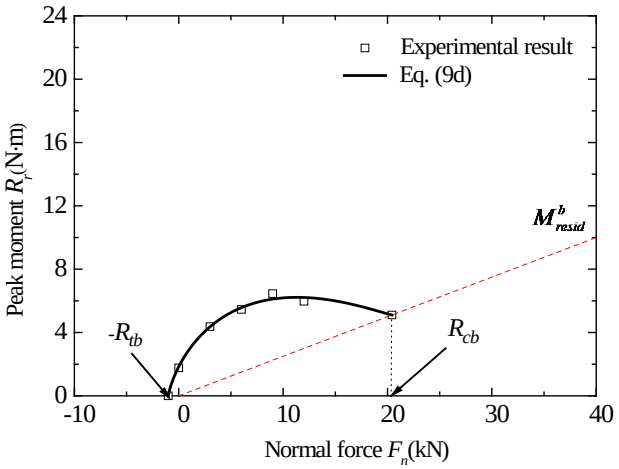

(b) Critical bond length 1.0mm

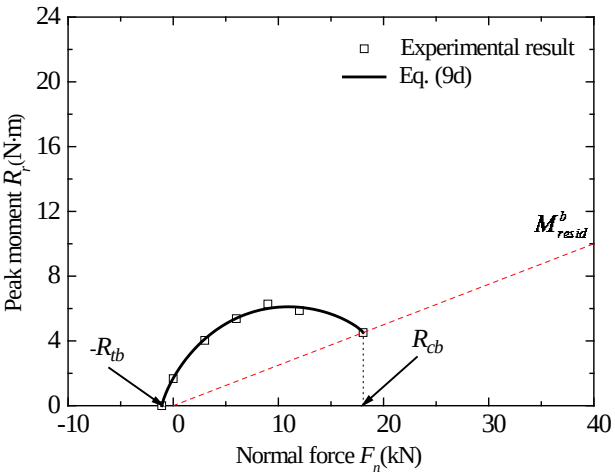

(c) Critical bond length 1.5mm

Figure 6. Rotational strength envelope of cement bond.

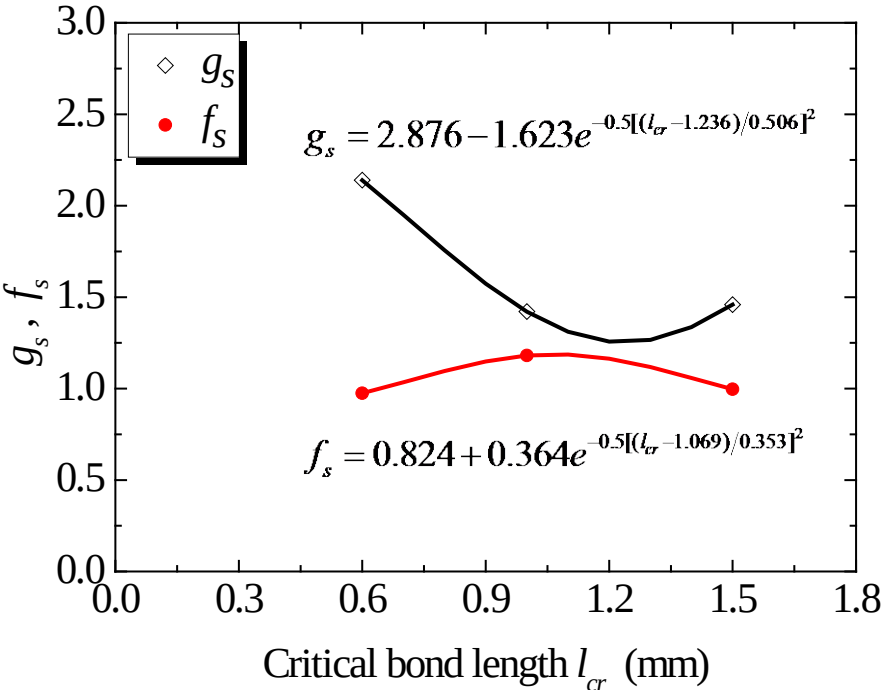

(a) Shear

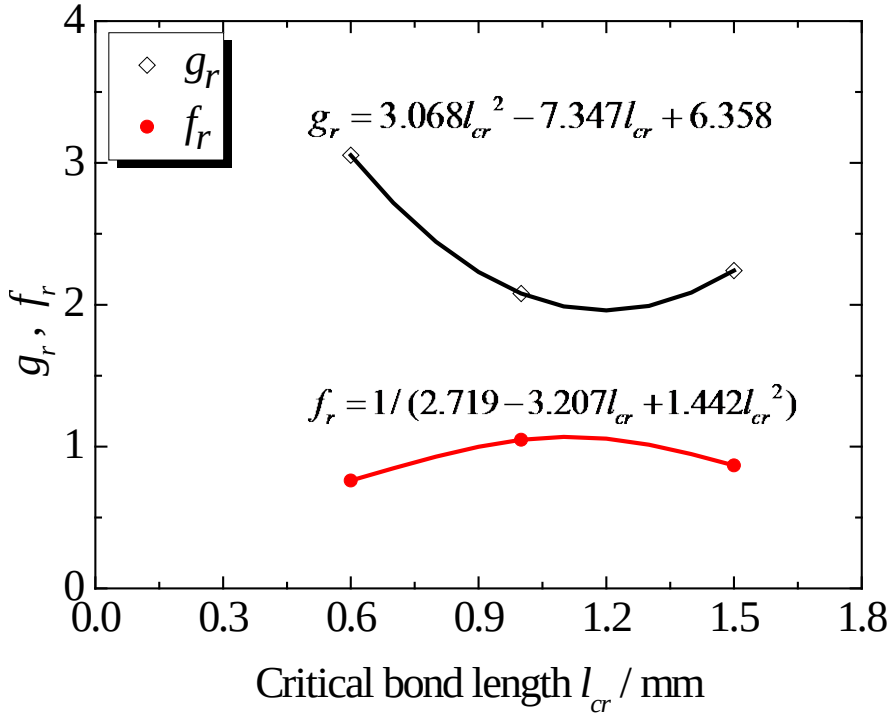

(b) Rotation

Figure 7. Fitting of strength envelope parameters.

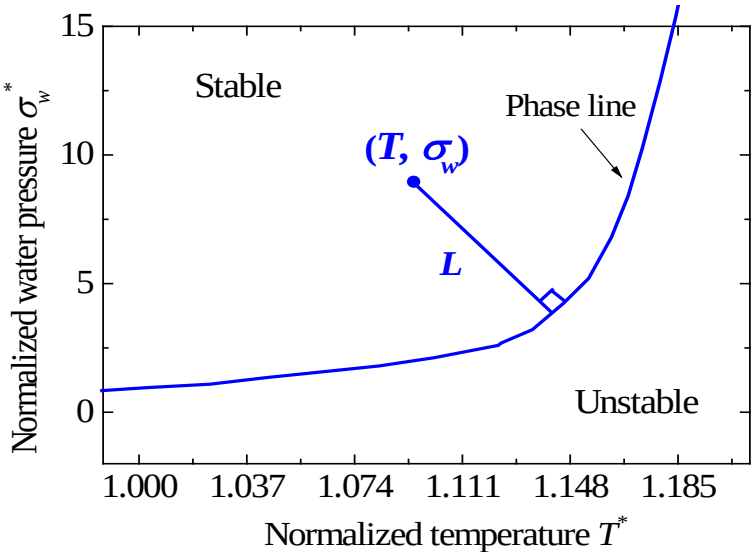

Figure 8. Phase equilibrium of MH (Sun et al., 2014).

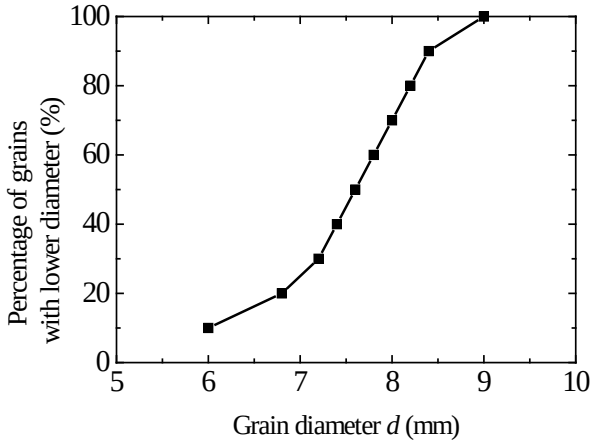

Figure 9. Grain size distribution for non-bonded soil specimens.

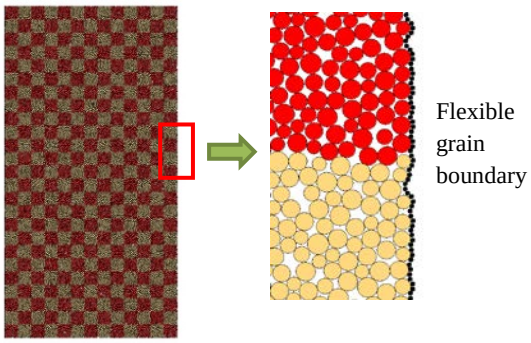

Figure 10. Flexible grain boundary in DEM and mosaic-style coloring.

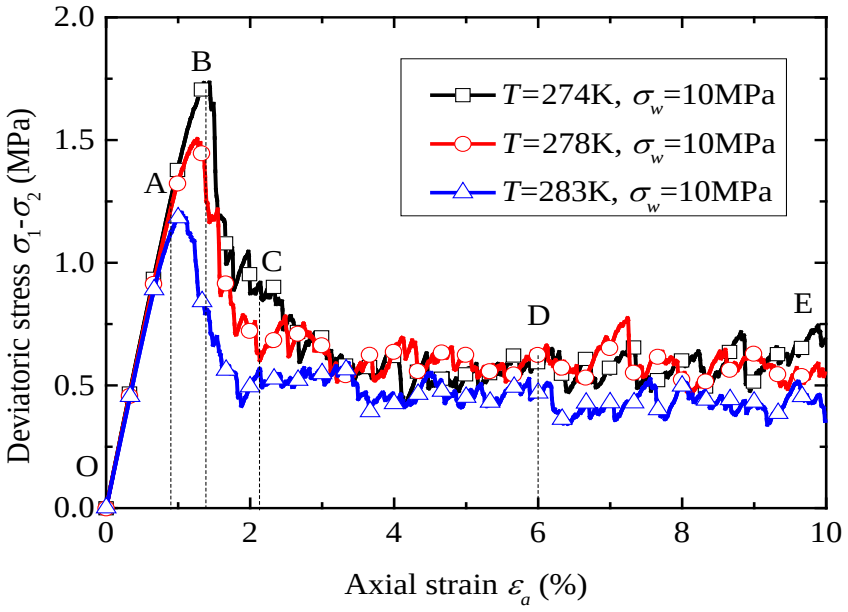

(a) Stress-strain relationship

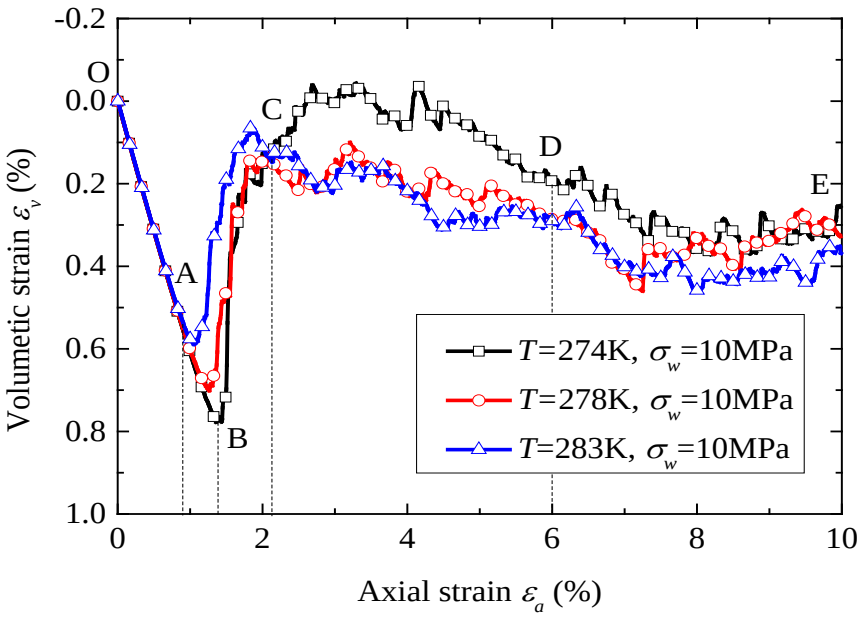

(b) Volumetric strain-axial strain relationship

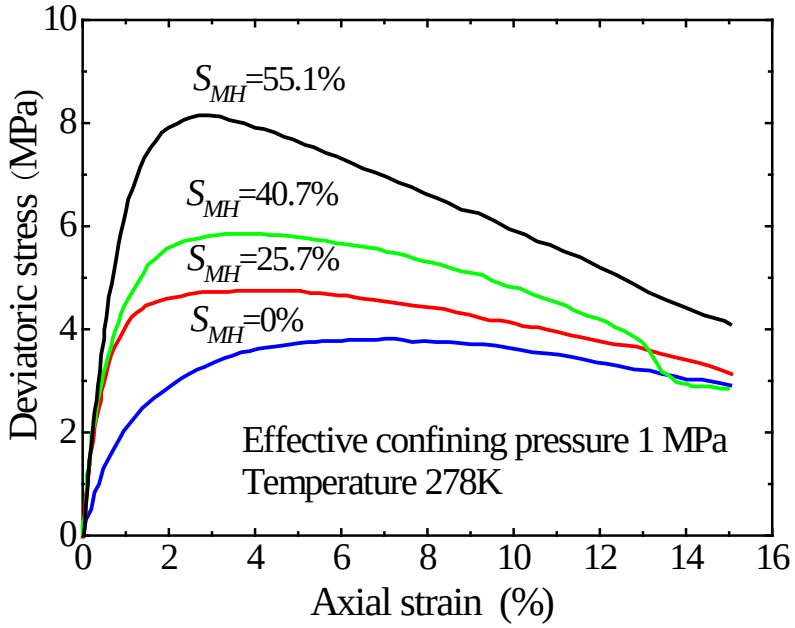

(c) Stress-strain relationship of MHBS acquired from experiments by Masui et al. (2005)

Figure 11. Variation of deviatoric stress and volumetric strain with axial strain for MHBS under different temperatures

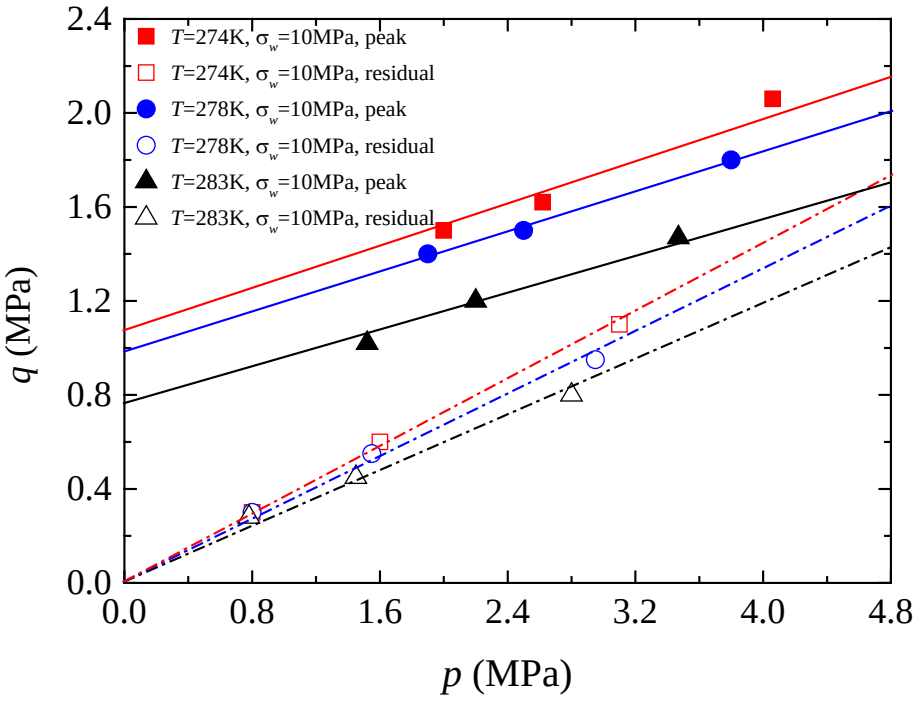

Figure 12. Strength envelope of MHBS under different temperatures.

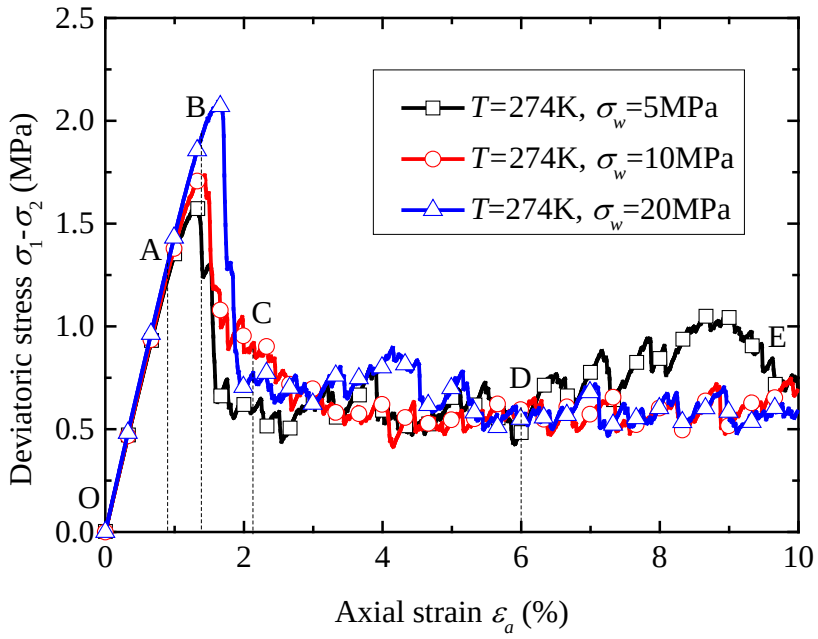

(a) Stress-strain relationship

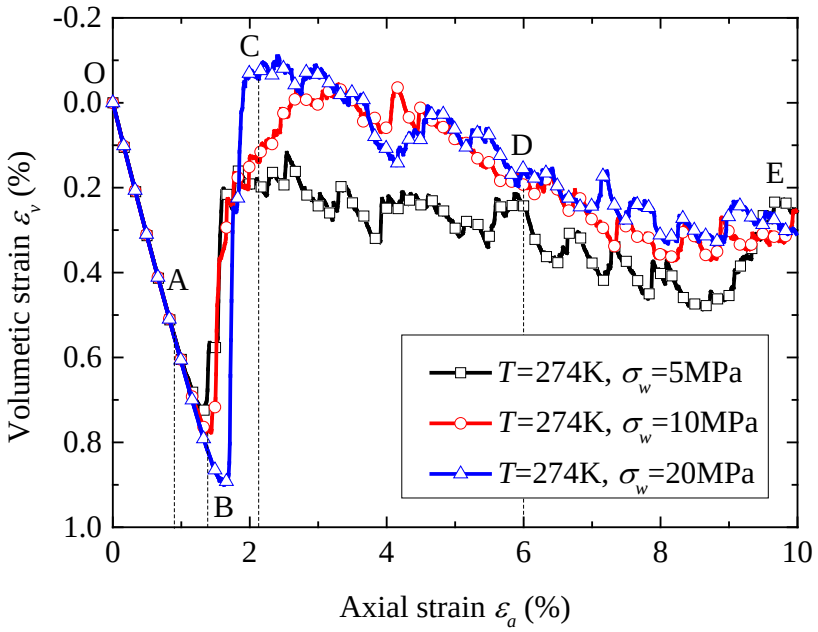

(b) Volumetric strain-axial strain relationship

Figure 13. Variation of deviatoric stress and volumetric strain with axial strain for MHBS under different water pressures.

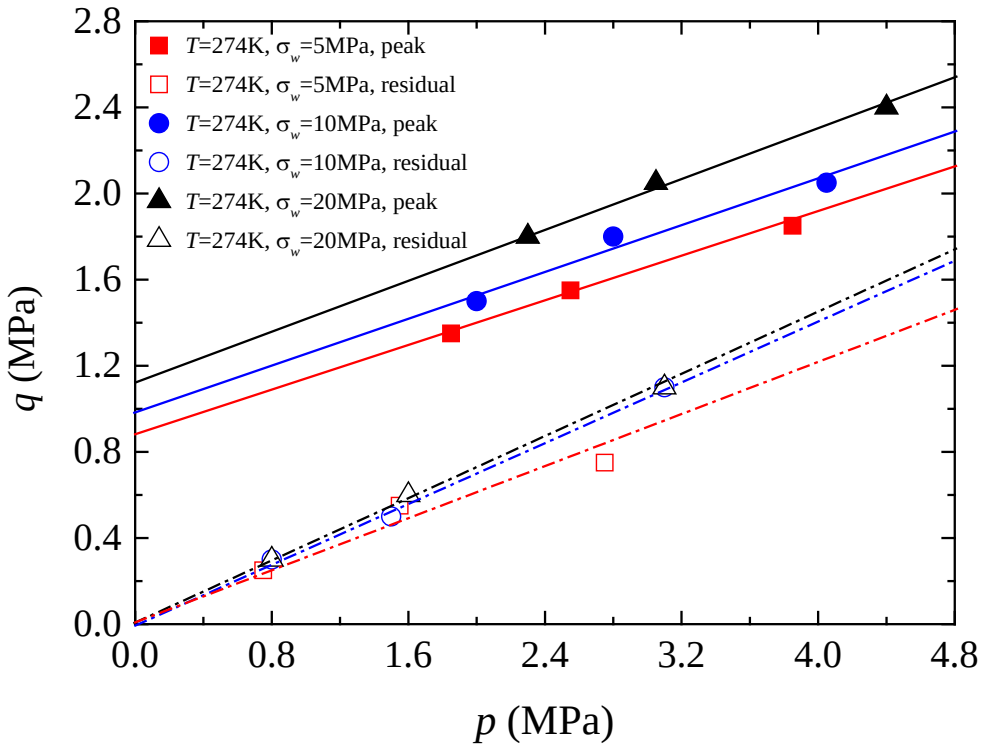

Figure 14. Strength envelope of MHBS under different water pressures.

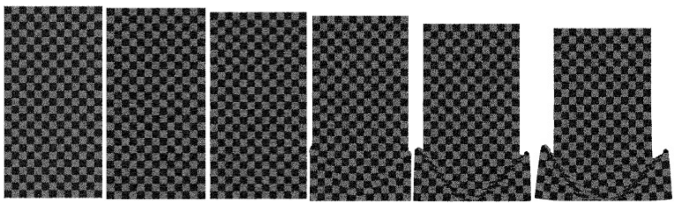

(a) T=274K, σ_w=5MPa (Type 1)

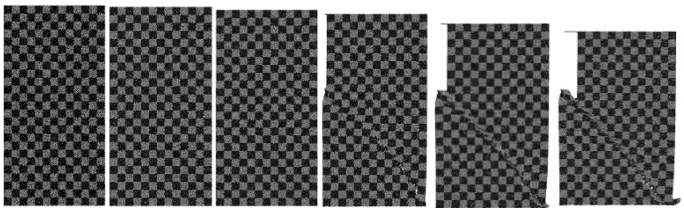

(b) T=274K, σ_w=10MPa (Type 2)

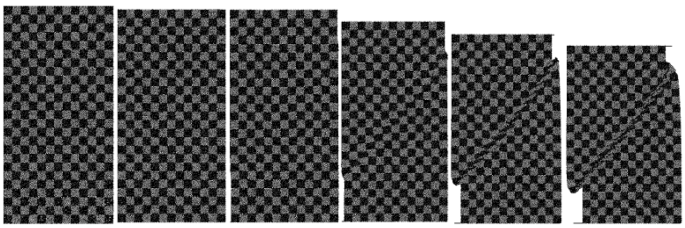

(c) T=283K, σ_w=10MPa (Type 3)

Figure 15. Deformation response during deviatoric loading for the three MHBS specimens.

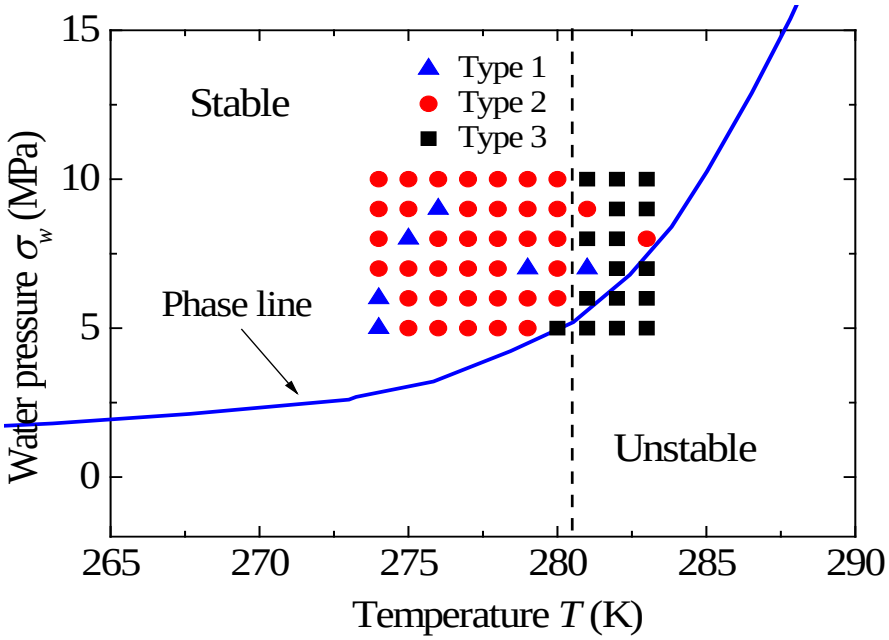

Figure 16. Different types of shear bands

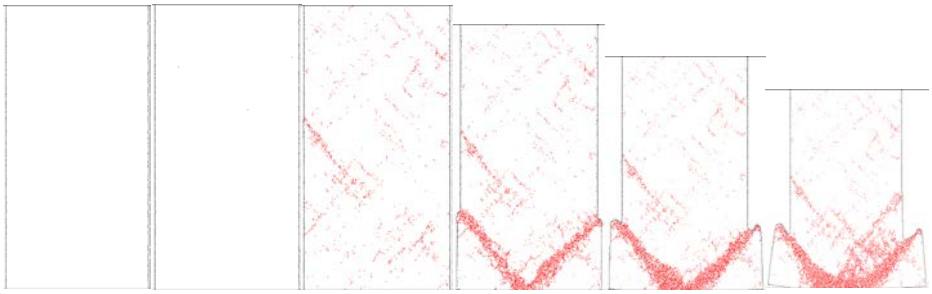

(a) T=274K, σ_w=5MPa (Type 1)

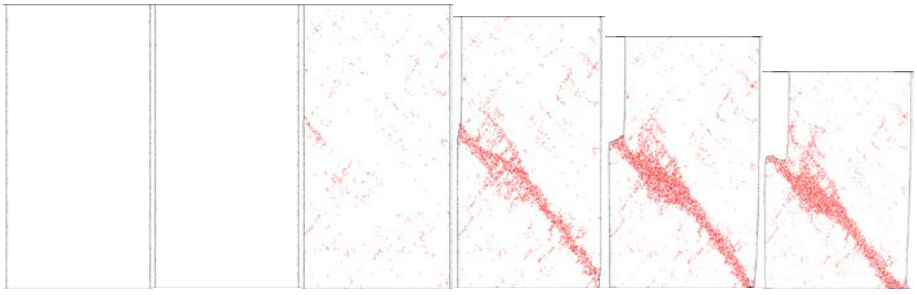

(b) T=274K, σ_w=10MPa (Type 2)

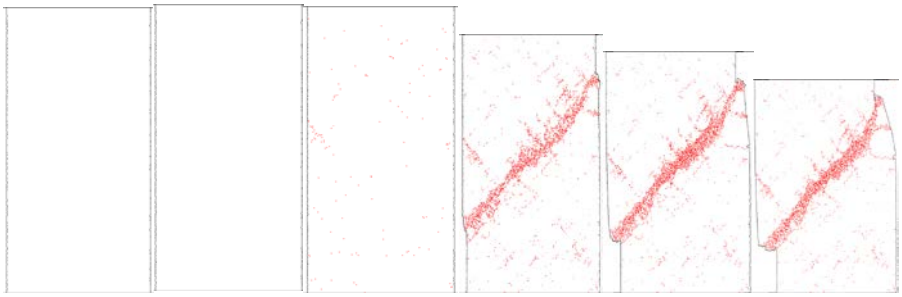

(c) T=283K, σ_w=10MPa (Type 3)

Figure 17. Bond breakage fields of three MHBS specimens.

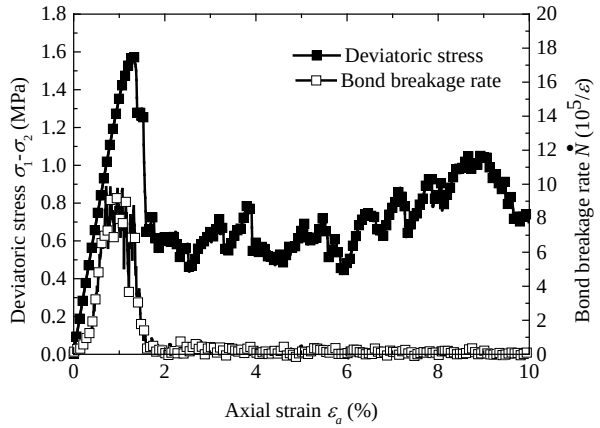

(a) T=274K, σ_w=5MPa

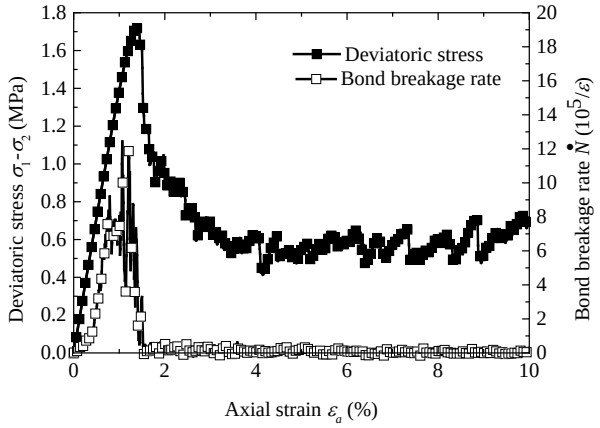

(b) T=274K, σ_w=10MPa

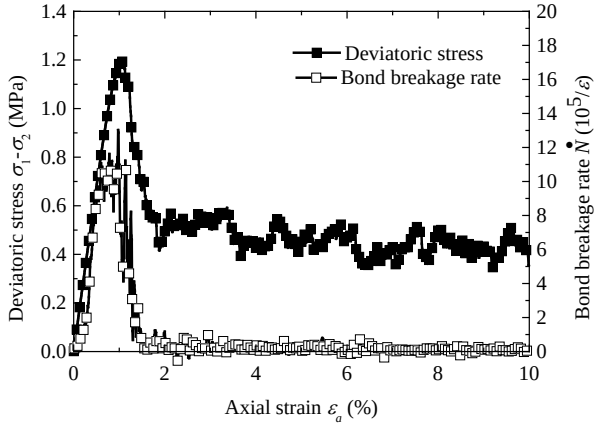

(c) T=283K, σ_w=10MPa

Figure 18. Stress-strain relationship and bond breakage-strain relationship of three MHBS specimens.

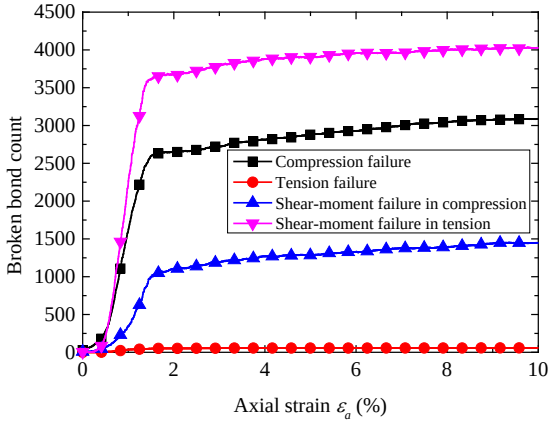

(a) T=274K, σ_w=5MPa (Type 1)

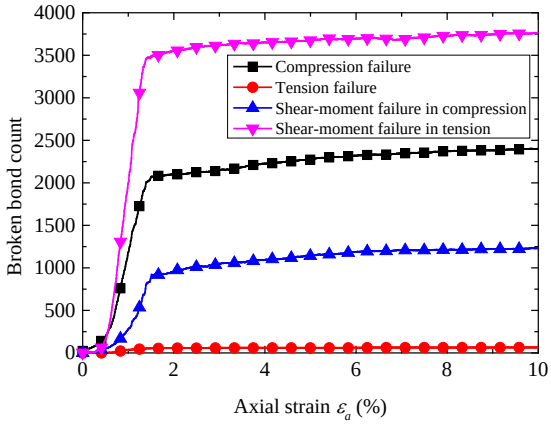

(b) T=274K, σ_w=10MPa (Type 2)

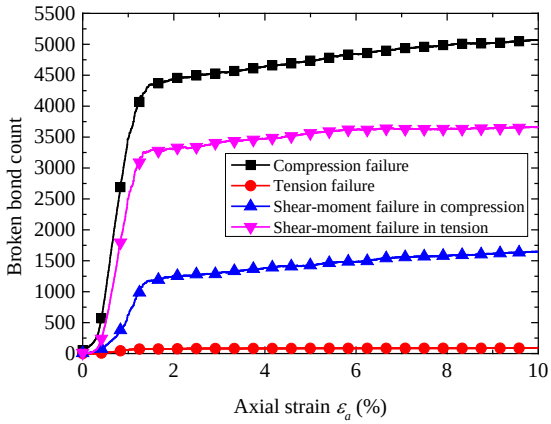

(c) T=283K, σ_w=10MPa (Type 3)

Figure 19. Number of bond failures in different modes for the three MHBS specimens.

	T and σ_w (Type)	O	A	B	C	D	E
Contact force chains	274K, 5MPa (Type 1)	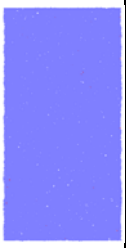			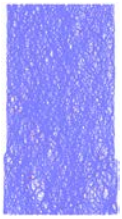	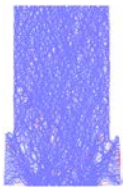	
	274K, 10MPa (Type 2)				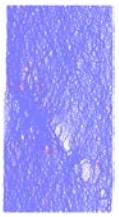	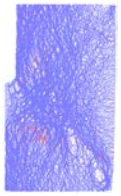	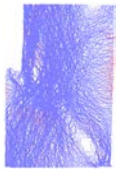
	283K, 10MPa (Type 3)				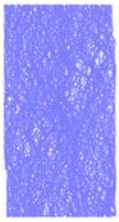	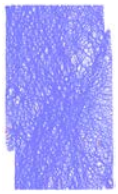	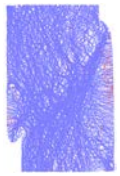
Principal stress fields	274K, 5MPa (Type 1)	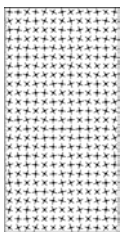	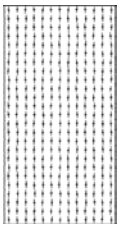	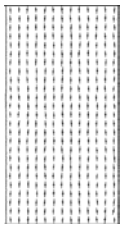	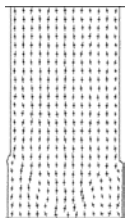	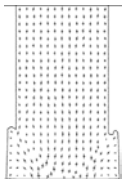	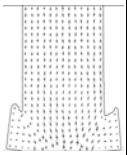
	274K, 10MPa (Type 2)	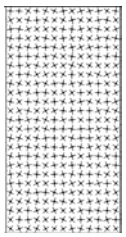	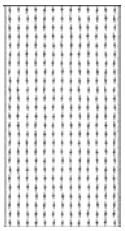	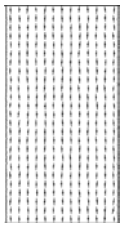	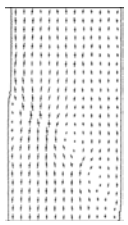	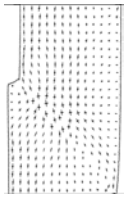	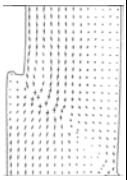
	283K, 10MPa (Type 3)	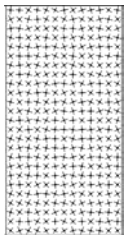	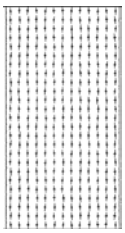	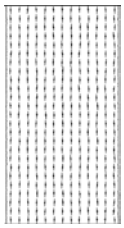	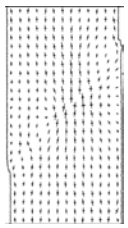	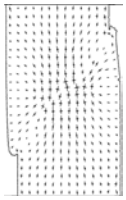	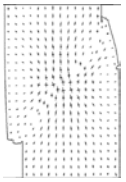

Particle velocity fields	274K, 5MPa (Type 1)	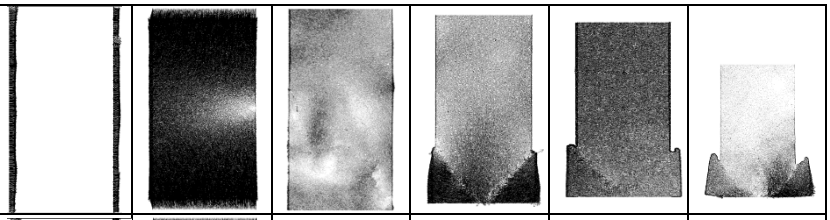					
	274K, 10MPa (Type 2)	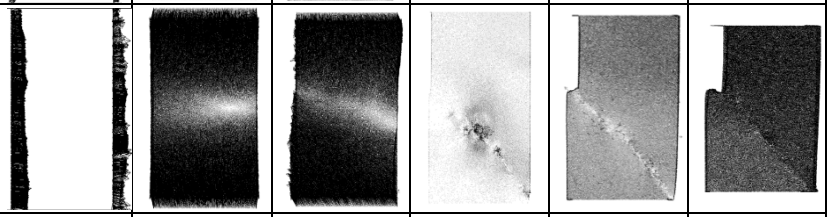					
	283K, 10MPa (Type 3)	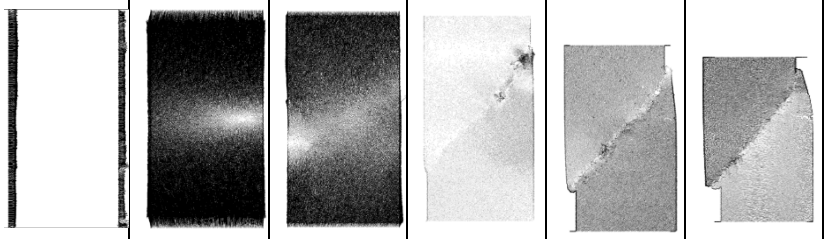					
APR distributions	274K, 5MPa (Type 1)	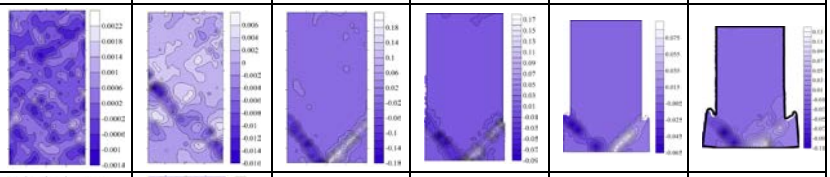					
	274K, 10MPa (Type 2)	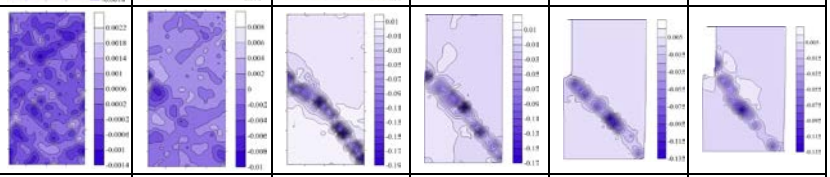					
	283K, 10MPa (Type 3)	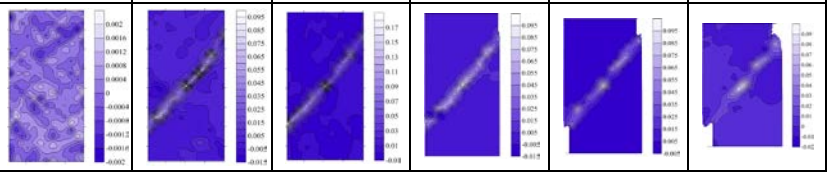					

Figure 20. Contact forces, principal stress fields, particle velocity fields and APR distributions of three MHBS specimens.

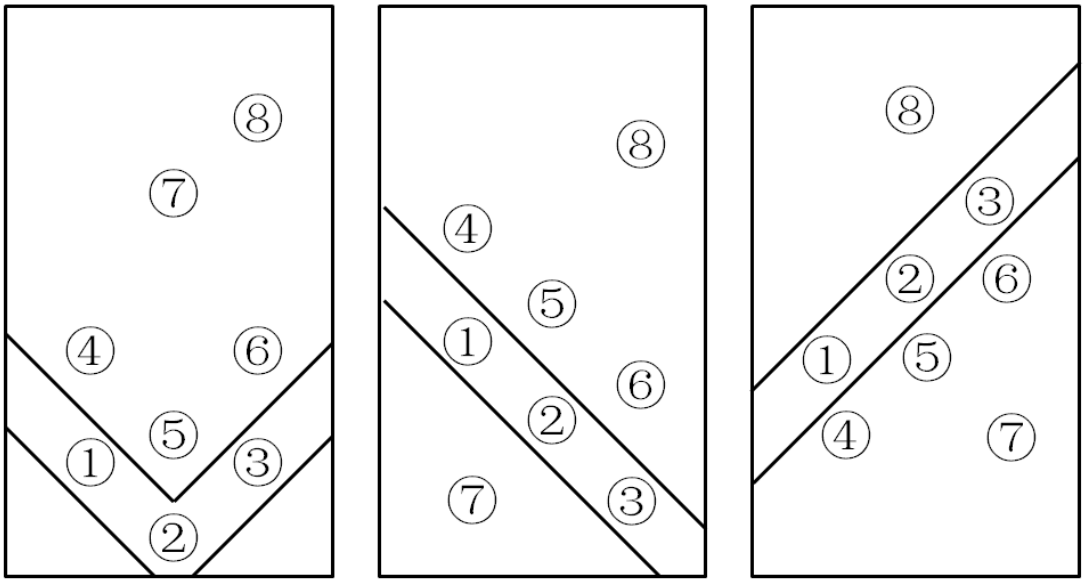

(a) Type 1 (b) Type 2 (c) Type 3

T=274K, σ_w=5MPa *T*=274K, σ_w=10MPa *T*=283K, σ_w=10MPa

Figure 21. Measurement circles in the three MHBS specimens.

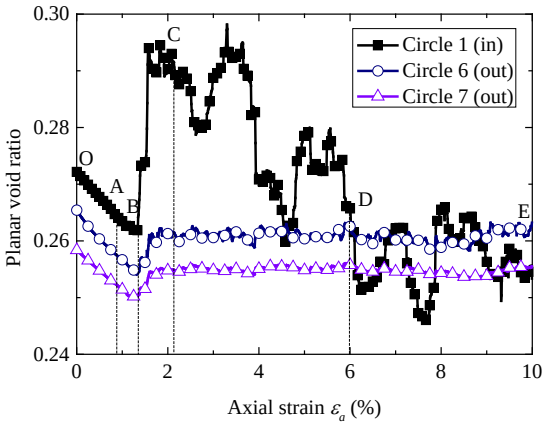

(i) T=274K, σ_w=5MPa (Type 1)

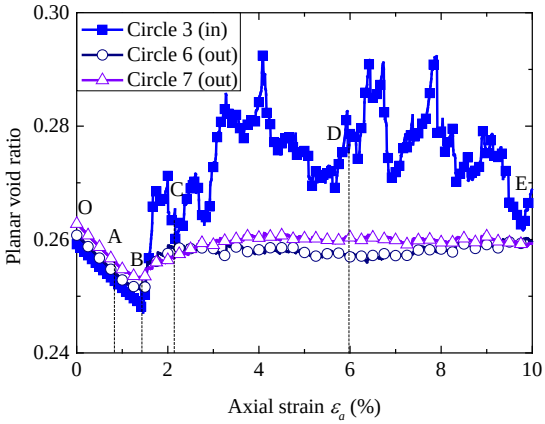

(ii) T=274K, σ_w=10MPa (Type 2)

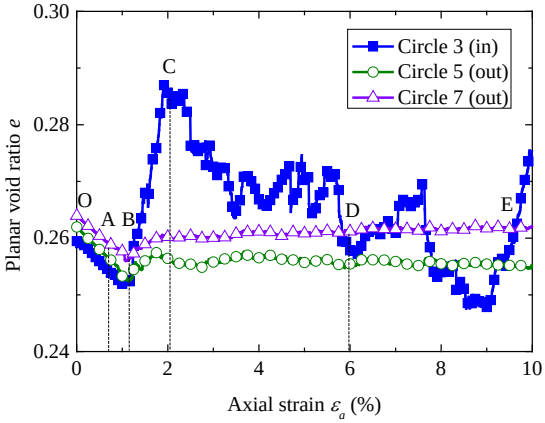

(iii) T=283K, σ_w=10MPa (Type 3)

(a) Void ratio

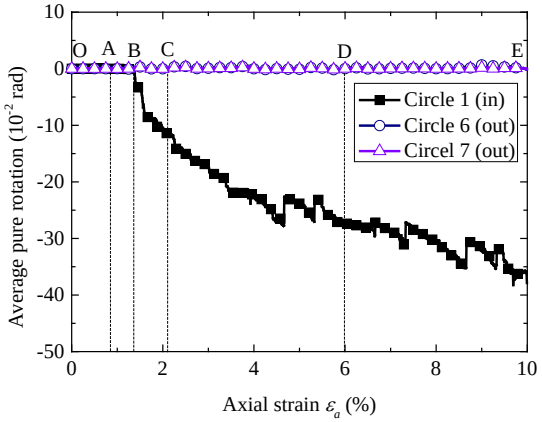

(i) T=274K, σ_w=5MPa (Type 1)

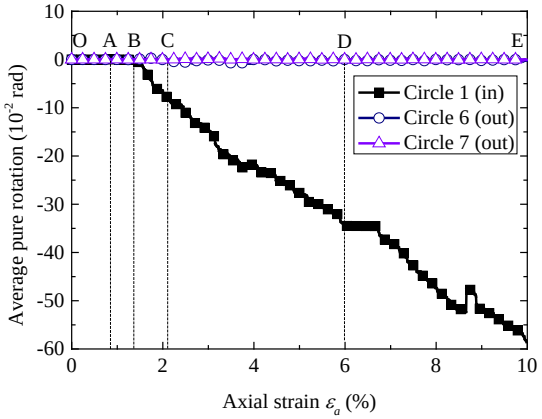

(ii) T=274K, σ_w=10MPa (Type 2)

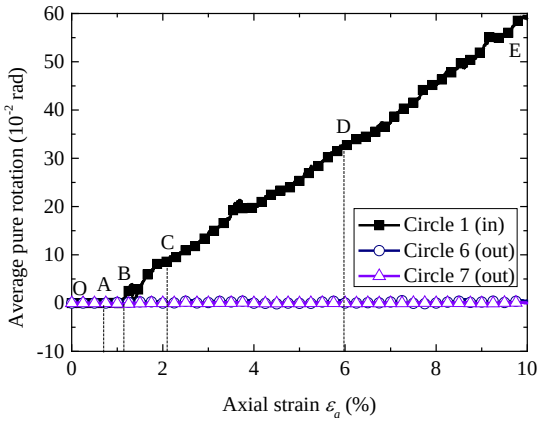

(iii) T=283K, σ_w=10MPa (Type 3)

(b) Pure rotation value

Figure 22. Evolution of void ratio and pure rotation value inside and outside the shear band in the three MHBS specimens.

Table 1. Values of fitting parameters of shear resistance envelope of Portland cement bond.

Critical bond length	0.6 mm	1.0 mm	1.5 mm
g_s	2.140	1.421	1.459
f_s	0.975	1.181	0.997

Table 2. Values of fitting parameters of shear resistance envelope of Portland cement bond.

Critical bond length	0.6 mm	1.0 mm	1.5 mm
g_r	3.054	2.079	2.241
f_r	0.761	1.048	0.867

Table 3. Sample parameters.

Size of the sample (mm, mm)	820 × 1640
Number of particles	24000
Planar void ratio e_p	0.27
Particle density ρ_s (kg/m^3)	2600
Particle normal stiffness k_n^p (N/m)	6.0×10^8
Particle shear stiffness k_s^p (N/m)	4.0×10^8
Particle friction coefficient μ^p	0.5
Boundary friction coefficient	0.0
Boundary normal stiffness (N/m)	3.0×10^{10}
Particle rolling resistance coefficient	0.5
Local damping coefficient	0.7
Viscous damping coefficient	0
MH density ρ (g/cm^3)	0.9
MH elastic modulus E	Function of T and σ_w see Eq. (11a)
MH compression strength σ_{cMH}	Function of T and σ_w see Eq. (11b)
MH tension strength σ_{tMH}	Function of T and σ_w see Eq. (11c)
MH bond friction coefficient μ^b	0.5
MH bond rolling resistance coefficient β^b	1.0
Critical length of MH bond l_{cr} (mm)	0.6
MH saturation (%)	53.2

Table 4. Cohesion and friction angle of MHBS with different temperatures.

Water pressure (MPa)	Temperature (K)	Cohesion at peak state (MPa)	Peak friction angle (°)	Residual friction angle (°)
10	274	1.05	15.21	20.61
	278	1.01	13.13	18.69
	283	0.69	12.35	17.83

Table 5. Cohesion and friction angle of MHBS with different water pressures.

Temperature (K)	Water pressure (MPa)	Coheasion (MPa)	Peak friction angles(°)	Residual friction angles(°)
274	5	0.93	14.34	17.14
	10	1.05	15.21	20.61
	20	1.21	16.41	21.09

Table 6. Thickness and inclination angle of shear band in the three MHBS specimens.

(a) Thickness

Temperature and water pressure (Type)	Evaluation criteria	Thickness (d_{50}) C: axial strain ε_a=2%	D: axial strain ε_a=6%	E:axial strain ε_a=10%
	Deformation pattern	11.91 / 10.96	13.72 / 13.47	15.66 / 17.48
T=274K,	Stress field	11.92 / 11.72	14.39 / 14.03	16.16 / 17.18
σ_w=5MPa	Distribution of bond breakage	12.05 / 11.73	15.12 / 14.73	15.24 / 17.60
(Type 1)	Distribution of APR	11.84 / 11.38	14.53 / 14.13	16.05 / 17.78
	Average thickness	11.93 / 11.45	14.44 / 14.09	15.78 / 17.51
	Deformation pattern	9.30	10.27	12.32
T=274K,	Stress field	9.05	10.98	13.10
σ_w=10MPa	Distribution of bond breakage	9.90	10.39	12.16
(Type 2)	Distribution of APR	9.62	10.49	12.73
	Average thickness	9.47	10.53	12.58
	Deformation pattern	13.58	14.97	19.31
T=283K,	Stress field	14.02	15.08	18.70
σ_w=10MPa	Distribution of bond breakage	10.66	14.57	17.39
(Type 3)	Distribution of APR	12.24	14.13	17.81
	Average thickness	12.63	14.69	18.30

(b) Inclination angles

Temperature and water pressure (Type)	Evaluation criteria	Inclination with respect to horizontal direction (deg.) C: axial strain ε_a=2%	D: axial strain ε_a=6%	E:axial strain ε_a=10%
T=274K, σ_w =5MPa (Type 1)	Deformation pattern	49 / 48	47 / 48	51 / 49
	Stress field	49 / 48	47 / 48	52 / 52
	Distribution of bond breakage	49 / 48	47 / 48	50 / 48
	Distribution of APR	49 / 48	47 / 48	50 / 47
	Average inclination	49 / 48	47 / 48	50.75 / 49
T=274K, σ_w =10MPa (Type 2)	Deformation pattern	47	48	46
	Stress field	47	47	47
	Distribution of bond breakage	46	47	48
	Distribution of APR	47	46	50
	Average inclination	46.75	47	47.75
T=283K, σ_w =10MPa (Type 3)	Deformation pattern	49	49	49
	Stress field	48	49	52
	Distribution of bond breakage	48	49	51
	Distribution of APR	49	49	48
	Average inclination	48.5	49	50